Cation-exchange synthesized Zn-doped Ag_2S Nanostructures for Photothermal and Photodynamic Therapies across Breast Cancer Subtypes

Harshavardhan Mohan[1], Satabdi Acharya[2], Inhee Chung[3*], Taeho Shin[1*]

***Corresponding authors.**

Harshavardhan Mohan**,** Taeho Shin **(shin@jbnu.ac.kr)**

Department of Chemistry, Research Institute of Physics and Chemistry, Jeonbuk National University, Jeonju 54896, Republic of Korea.

Satabdi Acharya

Department of Medical Science, Jeonbuk National University, Jeonju 54896, Republic of Korea.

Inhee Chung **(inheec@gwu.edu)**

Department of Anatomy and Cell Biology, School of Medicine and Health Sciences, George Washington University, Washington, DC, USA

Short title: *$Zn_xAg_{2-2x}S$ (ZSS) for efficient photodynamic/thermal activity*

****Disclaimer**: This preprint is not peer reviewed. The content may be revised upon peer review and/or acceptance.**

ABSTRACT

Photothermal therapy (PTT) and photodynamic therapy (PDT) require nanostructures with strong near-infrared (NIR) absorption, efficient charge separation, and biocompatibility, yet most current systems are limited by modest photothermal conversion and reactive oxygen species (ROS) yield. Silver sulfide (Ag_2S) is a promising NIR-responsive candidate, but its therapeutic performance remains suboptimal. Here, we report zinc doped Ag_2S (ZSS) nanostructures, synthesized via controlled cation exchange, that exhibit tunable electronic structure, enhanced NIR absorption, and improved carrier dynamics. Among the series, ZSS(0.15) demonstrated optimal bandgap narrowing, a high photothermal conversion efficiency of 67.26%, and markedly increased ROS generation under 660 nm excitation. These physicochemical enhancements translated into potent therapeutic outcomes: *in-vitro*, ZSS(0.15) reduced the IC_{50} to 15 μg/mL and induced 62.4% apoptosis via activation of the p53/Bax/Caspase pathway. *In-vivo*, ZSS(0.15) combined with laser irradiation achieved ~97% tumor volume suppression without systemic toxicity. Extending evaluation across multiple breast cancer subtypes (MCF-7, MDA-MB-231, SK-BR-3, T47D) further confirmed broad-spectrum efficacy. This work introduces a lattice-engineered Zn/Ag_2S nanoplatform that couples materials innovation with synergistic PTT/PDT, offering a versatile route toward clinically relevant cancer nanomedicines.

Keywords: Apoptosis; Breast cancer; ROS; Synergistic PTT/PDT; Zn-doped Ag_2S.

1. INTRODUCTION

Breast cancer remains one of the leading causes of cancer-related mortality in women worldwide [1]. Despite advances in chemotherapy, radiotherapy, and targeted molecular interventions, current treatments are constrained by systemic toxicity, limited tumor specificity, and the emergence of multidrug resistance [2]. The non-specific biodistribution of therapeutic agents and the accumulation of off-target toxicities not only reduce treatment efficacy but also compromise patient quality of life [3]. While conventional approaches can achieve disease control in certain cases, they frequently fail to fully eradicate tumors, thereby increasing the risk of recurrence [4, 5]. These limitations highlight the urgent need for alternative, minimally invasive treatment modalities that combine tumor-specific targeting with reduced collateral damage to healthy tissues.

Light-based therapies have emerged as attractive solutions to these challenges, offering spatial and temporal control of treatment with minimal side effects [6]. In particular,

photothermal therapy (PTT) and photodynamic therapy (PDT) are considered synergistic and highly promising non-invasive approaches with reduced systemic toxicity [7]. PTT induces localized hyperthermia via light-activated photothermal agents, whereas PDT relies on photosensitizers to generate reactive oxygen species (ROS), including singlet oxygen ($^1O_2$), superoxide anions (O_2^{*-}), and hydroxyl radicals ($^*OH$), which disrupt cellular redox homeostasis and trigger apoptotic cascades [8, 9]. Recent progress in nanotechnology has enabled the design of multifunctional nanomaterials that integrate both PTT and PDT into a single therapeutic platform. Among these, silver sulfide (Ag_2S) nanostructures are particularly promising due to their strong near-infrared (NIR) absorbance, high photostability, and relatively low toxicity [10-12]. Recent progress in nanotechnology has enabled the design of multifunctional nanomaterials that integrate both PTT and PDT into a single therapeutic platform. Among these, silver sulfide (Ag□S) nanostructures are particularly promising due to their strong near-infrared (NIR) absorbance, high photostability, and relatively low toxicity [13, 14]. For instance, Liu et al. [15] demonstrated a tumor-inhibiting Ag_2S based nanoplatform with substantial tumor reduction, but the system still required improvements in synthesis simplicity and overall therapeutic efficacy.

One effective strategy to overcome these shortcomings is metal-ion doping, which modulates the optical, electronic, and photothermal properties of Ag_2S. Although various dopants have been investigated, many raise concerns regarding biosafety and long-term *in vivo* compatibility [16]. Zinc presents a particularly attractive alternative due to its essential biological role, low cytotoxicity at therapeutic doses, and documented metabolic clearance pathways. [17]. Moreover, Zn^{2}□ incorporation into semiconductor lattices is known to induce lattice distortions and tune the bandgap, thereby promoting efficient charge separation and suppressing radiative recombination key factors for improving both light-to-heat conversion and ROS generation [18]. Despite these advantages, the therapeutic potential of Zn-doped Ag_2S nanostructures has not been systematically investigated.

In this study, we synthesized and characterized Zn-doped Ag_2S (ZSS) nanostructures with systematically varied doping levels (Zn:Ag, 0.0 to 0.30) to identify the optimal composition that balances structural integrity, charge separation, and therapeutic efficacy under 660 nm NIR irradiation. The objectives were to elucidate the physicochemical and photo-responsive behavior of ZSS nanostructures, evaluate their ROS-mediated cytotoxicity, and investigate the underlying mechanistic pathways *in-vitro* and *in-vivo*. To establish broad spectrum relevance, the therapeutic potential was assessed across multiple breast cancer cell

lines representing distinct molecular subtypes [19, 20]: luminal A (MCF-7, T47D), HER2-positive (SK-BR-3), and triple-negative (MDA-MB-231). This integrated approach not only advances understanding of doped nanomaterials in cancer nanomedicine but also introduces a highly effective and previously unexplored Zn-engineered Ag_2S platform for clinical translation in non-invasive cancer therapy.

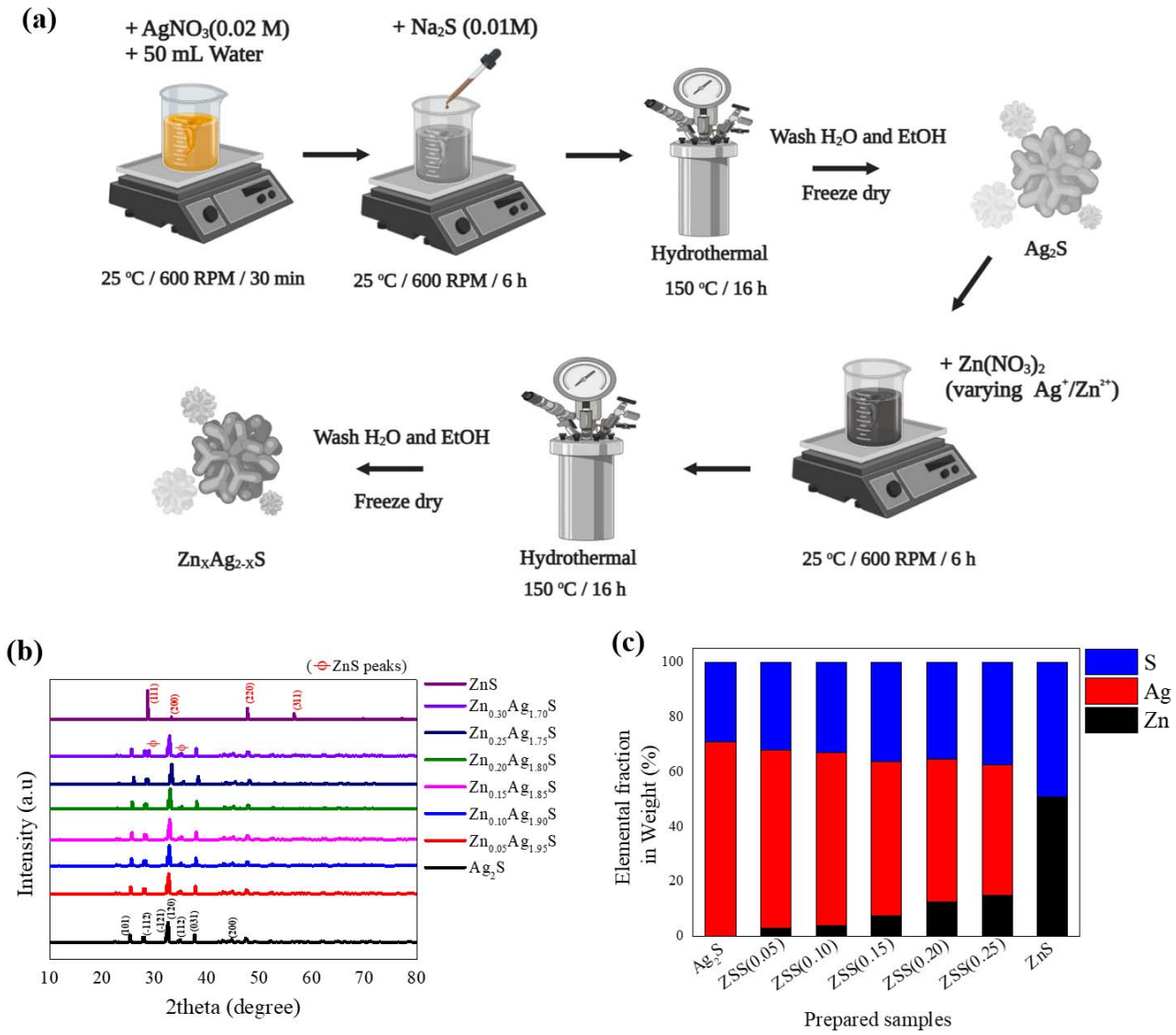

Figure 1 **(a)** Schematic illustration of the synthesis procedure for $Zn_xAg_{2-2x}S$ (ZSS) nanostructures; **(b)** XRD patterns of the synthesized ZSS samples; **(c)** Elemental composition (wt%) obtained from ICP-OES analysis.

2. RESULTS AND DISCUSSION

2.1. Structural and compositional characterization

2.1.1. XRD

The crystallographic features of the synthesized $Zn_xAg_{2-2x}S$ (ZSS) hybrid nanostructures (**Figure 1a**) with varying Zn-to-Ag ratios (x = 0.05–0.30) were investigated using X-ray diffraction (XRD, MiniFlex 600, Korea I.T.S Co., Ltd), as shown in **Figure 1b**. The pristine Ag_2S sample exhibited characteristic orthorhombic acanthite phase peaks indexed to (101), (−112), (−121), (120), (112), (031), and (200) planes (JCPDS No. 14-0072), confirming phase purity [21]. Conversely, the ZnS sample displayed a cubic zinc blende phase with diffraction peaks corresponding to (111), (200), (220), and (311) planes (JCPDS No. 05-0566), consistent with its well-known crystal structure [22]. Upon progressive substitution of Zn^{2+} into the Ag_2S lattice (ZSS(0.05) - ZSS(0.30)), all samples up to ZSS(0.25) retained the orthorhombic Ag_2S phase with no secondary phases detected, suggesting successful solid-state incorporation of Zn^{2+} ions without significant lattice distortion. However, at a Zn:Ag ratio of 0.30:1.70 (ZSS(0.30)), additional peaks matching the ZnS phase emerged, indicating phase segregation and a solubility threshold beyond which excess Zn precipitates out as a secondary ZnS phase. Therefore, ZSS(0.25) was identified as the optimal doping concentration that maintained single-phase hybrid integrity while enabling effective compositional tuning. The phase-pure nature of ZSS is critical for maintaining homogeneous energy band structures and interfacial charge transfer pathways, which directly influence its photophysical and therapeutic properties, as discussed in subsequent sections. The absence of secondary phases in ZSS(0.05) - ZSS(0.25) suggests a well-integrated substitutional doping mechanism, where Zn^{2+} ions, owing to their smaller ionic radius (0.74 Å) compared to Ag^+ (1.15 Å), substitute Ag^+ sites without significantly distorting the host lattice [22]. Notably, the gradual shift and slight broadening of diffraction peaks with increasing Zn content (especially visible between ZSS(0.10) - ZSS(0.25)) indicate minor lattice compression, affirming successful Zn incorporation and nanoscale crystallinity. These findings validate the rational design strategy adopted in this study, where phase purity was prioritized to ensure predictable and improved photothermal and photodynamic behavior.

2.1.2. ICP-OES

To verify the successful incorporation of Zn into the Ag_2S lattice and to quantify the elemental distribution, inductively coupled plasma optical emission spectroscopy (ICP-OES

(Agilent 5800)) was performed for all synthesized samples, as shown in **Figure 1c**. The pristine Ag_2S sample exhibited a binary composition of Ag and S with no detectable Zn content, consistent with its nominal stoichiometry. With the gradual incorporation of Zn (ZSS(0.05) - ZSS(0.25)), a clear trend of increasing Zn weight percentage was observed, accompanied by a proportional decrease in Ag content. This confirms the intended cation exchange between Ag and Zn ions, supporting the substitutional doping strategy. For instance, ZSS(0.05) and ZSS(0.10) showed minor Zn incorporation (<5 wt%), reflecting a low but successful doping level. As the Zn ratio increased, samples ZSS(0.15) and ZSS(0.20) demonstrated moderate Zn contents (~10-15 wt%) with a corresponding reduction in Ag, suggesting a balanced doping regime. Notably, ZSS(0.25) exhibited the highest Zn incorporation (~20 wt%) while retaining significant Ag, consistent with its XRD pattern indicating a single-phase solid solution without phase segregation. In contrast, the ZnS reference showed a complete absence of Ag, confirming its phase purity. The progressive elemental shift from Ag-rich to Zn-rich compositions across the ZSS series aligns well with the designed stoichiometric ratios. These quantitative findings complement the structural insights from XRD, further validating the formation of compositionally tunable $Zn_xAg_{2-2x}S$ hybrids.

2.1.3. TEM-EDS

To gain insight into the structural features and elemental distribution of the ZSS hybrids, transmission electron microscopy (TEM, Hitachi JEOL-2010 HR-TEM.) and energy-dispersive X-ray spectroscopy (EDS) analyses were performed for ZSS(0.15) as presented in **Figure 2**. Low-magnification TEM images (**Figure 2a-b**) reveal a crumpled, petal-like morphology indicative of ultrathin, wrinkled nanosheets aggregated into hierarchical flower-like structures. High-resolution TEM (**Figure 2c**) highlights the crystalline lattice fringes with an interplanar spacing of 0.330 nm, corresponding to the (101) plane of the Ag_2S crystal structure. These results support the well-defined crystallinity and anisotropic growth of the ZSS(0.15) nanostructures. The selected area electron diffraction (SAED) pattern (**Figure 3d**) exhibits multiple concentric rings indexed to the (101), (112), (120), (103), and (220) planes, confirming the polycrystalline nature of the material, complementing XRD data (**Figure 1b**). The bright-field scanning TEM image (**Figure 2e**) further supports the 3D interconnected nanosheet architecture. Elemental mapping through EDS (**Figures 2f-h**) clearly shows the homogeneous distribution of Zn (red), Ag (cyan), and

S (green) throughout the structure, signifying successful doping and uniform incorporation of Zn into the Ag_2S matrix without phase segregation. The EDS quantification table confirms an atomic composition of Zn: 7.49%, Ag: 56.26%, and S: 36.25%, consistent with the intended stoichiometry and the ICP-OES data (**Figure 1c**). TEM-derived size statistics (n = 75), as shown in **Figure SF1**, exhibit a Gaussian distribution with a dominant peak centered around 160 nm, indicating a relatively narrow size distribution. Most of the nanostructures fall within the 140-180 nm range, confirming the formation of uniformly distributed ZSS nanoflowers. This size range is ideal for biomedical applications, especially for enhanced tumor accumulation via the enhanced permeability and retention effect, while still small enough to promote efficient cellular uptake [23].

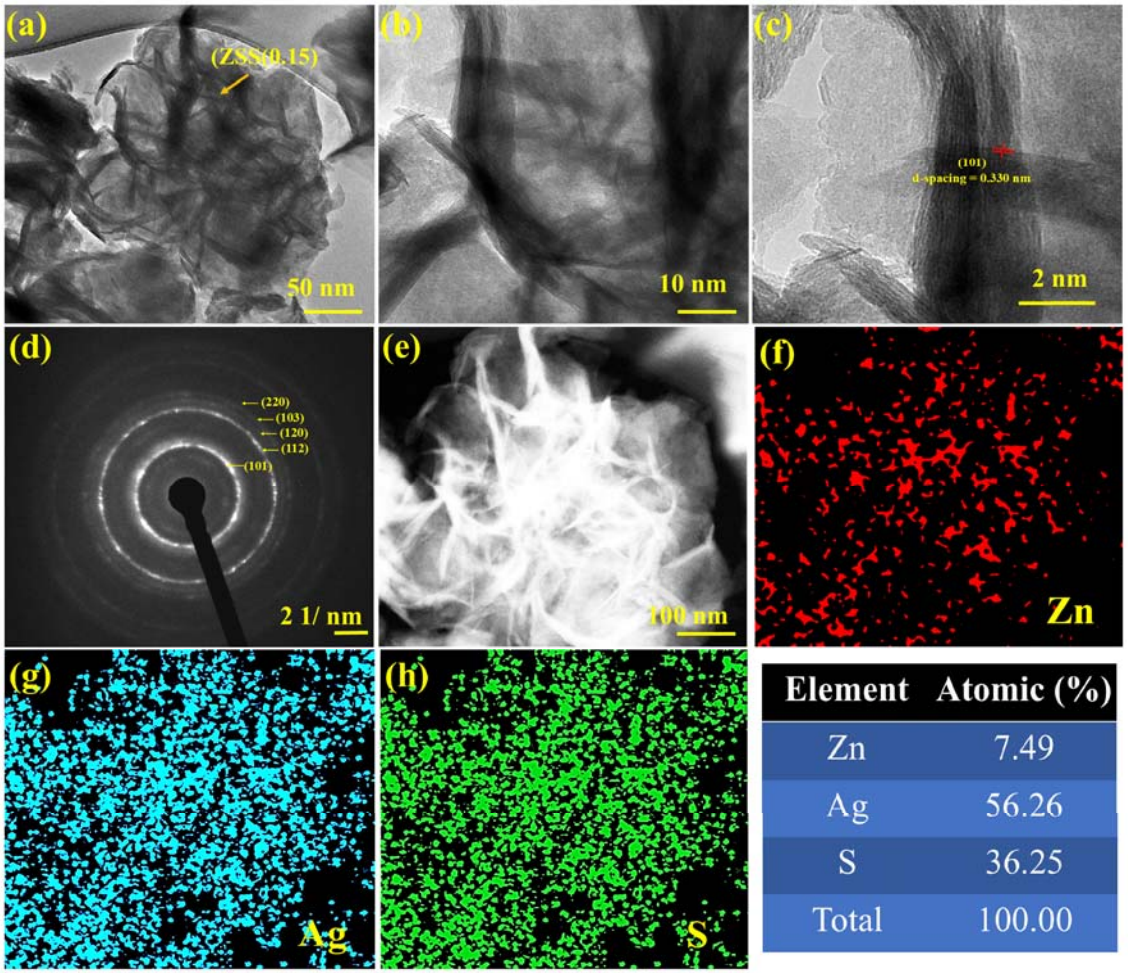

Element	Atomic (%)
Zn	7.49
Ag	56.26
S	36.25
Total	100.00

Figure 2 (a, b) Low-magnification TEM images of ZSS(0.15) nanostructures; **(c)** High-resolution TEM (HRTEM) image; **(d)** Corresponding SAED pattern; **(e)** Bright-field STEM image; **(f–h)** Elemental mapping of Zn, Ag, and S obtained from EDS analysis.

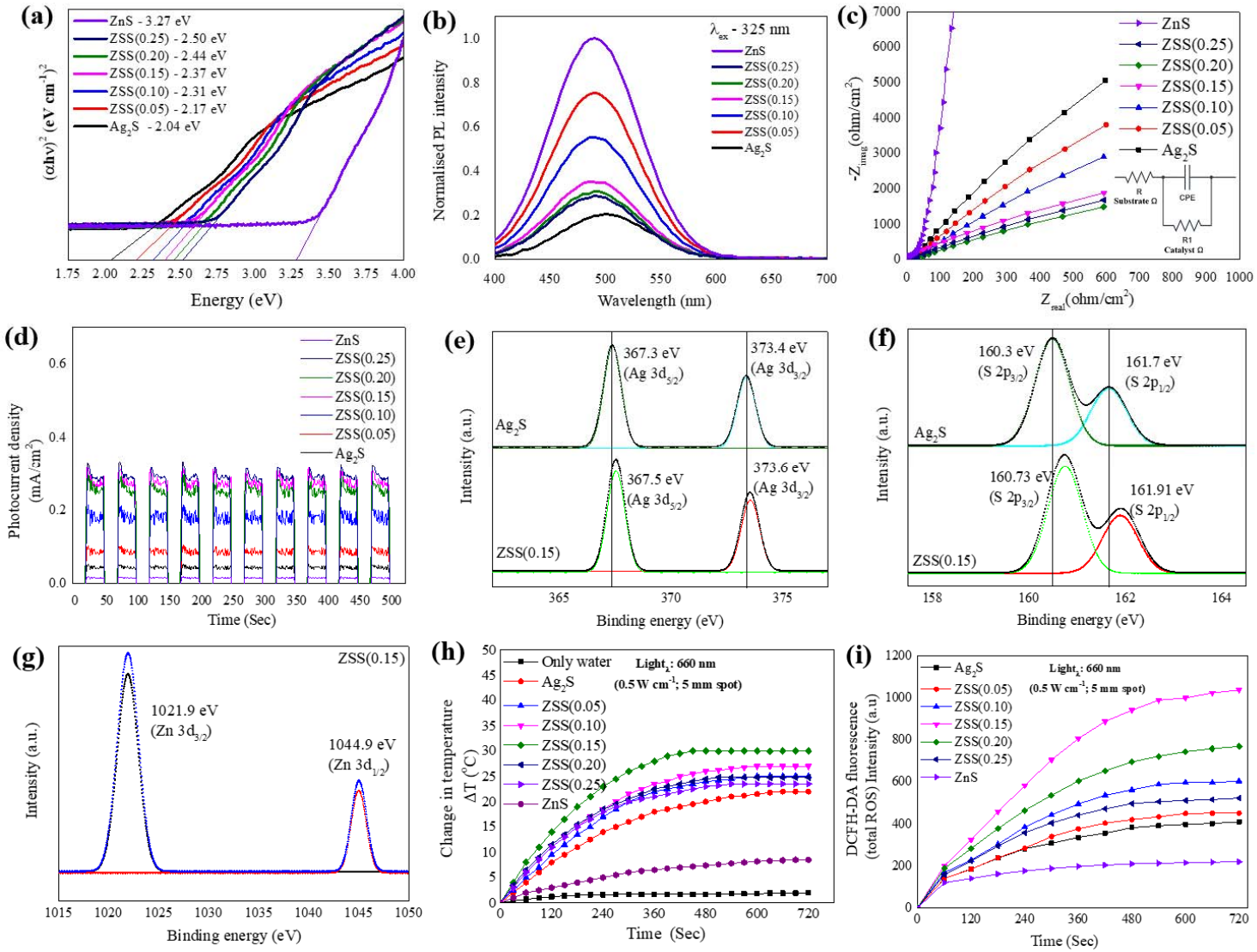
(a)
ZnS - 3.27 eV
ZSS(0.25) - 2.50 eV
ZSS(0.20) - 2.44 eV
ZSS(0.15) - 2.37 eV
ZSS(0.10) - 2.31 eV
ZSS(0.05) - 2.17 eV
Ag2S - 2.04 eV
(αhν)² (eV cm⁻¹)²
Energy (eV)
(b)
λex - 325 nm
ZnS
ZSS(0.25)
ZSS(0.20)
ZSS(0.15)
ZSS(0.10)
ZSS(0.05)
Ag2S
Normalised PL intensity
Wavelength (nm)
(c)
ZnS
ZSS(0.25)
ZSS(0.20)
ZSS(0.15)
ZSS(0.10)
ZSS(0.05)
Ag2S
R Substrate Ω
CPE
R1 Catalyst Ω
-Z_imag (ohm/cm²)
Z_real (ohm/cm²)
(d)
ZnS
ZSS(0.25)
ZSS(0.20)
ZSS(0.15)
ZSS(0.10)
ZSS(0.05)
Ag2S
Photocurrent density (mA/cm²)
Time (Sec)
(e)
367.3 eV (Ag 3d5/2)
373.4 eV (Ag 3d3/2)
Ag2S
367.5 eV (Ag 3d5/2)
373.6 eV (Ag 3d3/2)
ZSS(0.15)
Intensity (a.u.)
Binding energy (eV)
(f)
160.3 eV (S 2p3/2)
161.7 eV (S 2p1/2)
Ag2S
160.73 eV (S 2p3/2)
161.91 eV (S 2p1/2)
ZSS(0.15)
Intensity (a.u.)
Binding energy (eV)
(g)
ZSS(0.15)
1021.9 eV (Zn 3d3/2)
1044.9 eV (Zn 3d1/2)
Intensity (a.u.)
Binding energy (eV)
(h)
Only water
Ag2S
ZSS(0.05)
ZSS(0.10)
ZSS(0.15)
ZSS(0.20)
ZSS(0.25)
ZnS
Light λ: 660 nm
(0.5 W cm⁻¹; 5 mm spot)
Change in temperature ΔT (°C)
Time (Sec)
(i)
Ag2S
ZSS(0.05)
ZSS(0.10)
ZSS(0.15)
ZSS(0.20)
ZSS(0.25)
ZnS
Light λ: 660 nm
(0.5 W cm⁻¹; 5 mm spot)
DCFH-DA fluorescence (total ROS) Intensity (a.u)
Time (Sec)

Figure 3 (a) UV–Vis diffuse reflectance spectra (DRS); **(b)** Photoluminescence (PL) spectra; **(c)** Electrochemical impedance spectroscopy (EIS) plots; **(d)** Transient photocurrent response; **(e–g)** High-resolution XPS spectra of Ag 3d, S 2p, and Zn 2p, respectively; **(h)** Photothermal heating curves; **(i)** ROS generation profiles of the prepared nanostructures.

2.2. Optical and Electronic Properties

2.2.1. DRS-UV

The optical properties of ZSS nanostructures were systematically investigated using UV-Vis diffuse reflectance spectroscopy (DRS-UV-NIR, Jasco V-770 UV-Vis-NIR), and the corresponding Tauc plot (**Figure 3a**) revealed a clear trend of bandgap modulation with increasing Zn content. As the Zn:Ag ratio increased from 0.00 to 0.25, the optical bandgap widened progressively from 2.04 eV (pure Ag_2S) to 2.50 eV, approaching the wider bandgap of ZnS (3.27 eV). This blue shift in the absorption edge arises from the incorporation of smaller Zn^{2+} ions into the Ag_2S lattice, inducing lattice strain and electronic structure perturbations that enhance quantum confinement effects [24, 25]. The tunability of the bandgap through Zn doping directly influences the light absorption profile, enabling optimization within the red to near-infrared region suitable for 660 nm irradiation used in PDT and PTT [26]. A moderately narrowed bandgap not only facilitates deeper tissue penetration by red light but also promotes efficient generation of ROS and photothermal conversion, both of which are critical for effective cancer therapy. Thus, the observed bandgap evolution offers a strategic handle to fine-tune light-harvesting capabilities and photonic responsiveness of the nanostructures for synergistic PDT/PTT applications.

2.2.2. Photoluminescence

The photoluminescence (PL, Horiba Fluoromax-4 spectrofluorometer) spectra of the ZSS nanostructures (**Figure 3b**), excited at 325 nm, reveal distinct emission intensity variations with progressive Zn incorporation, reflecting the evolution of charge carrier dynamics. Pure ZnS exhibits the highest PL intensity, indicative of high radiative recombination rates, whereas pure Ag_2S shows the lowest intensity, suggesting efficient charge separation. As Zn doping increases, a non-linear trend emerges, with initial doping (e.g., ZSS(0.05)) leading to increased PL due to defect-related trap states, while higher doping levels (e.g., ZSS(0.15) - ZSS(0.25)) result in PL quenching. This reduction in

emission intensity at moderate-to-high Zn content signifies suppressed electron–hole recombination, likely owing to enhanced charge delocalization and defect passivation [27]. Such behavior is highly desirable for both photodynamic and photothermal therapy, as lower recombination rates prolong the lifetime of photogenerated charge carriers, thereby facilitating more efficient ROS generation and thermal energy conversion [28]. These findings confirm that rational band engineering via Zn substitution can strategically manipulate carrier dynamics, optimizing the nanostructures for dual-modal PDT/PTT cancer therapeutic applications.

2.2.3. EIS

Electrochemical impedance spectroscopy (EIS, ZIVE SP1, WonATech, Korea, with a standard three-electrode system) analysis was employed to investigate the interfacial charge transfer characteristics of the ZSS nanostructures (**Figure 3c**), with the Nyquist plots clearly highlighting significant differences in charge transfer resistance (R_{ct}) among the samples. Pure ZnS exhibited the largest semicircle, corresponding to the highest R_{ct}, which reflects its inherently poor conductivity and sluggish interfacial charge transfer. Conversely, Ag_2S displayed markedly lower resistance, indicative of improved electrical conductivity [29]. Upon Zn incorporation, a progressive decline in R_{ct} was observed up to a certain doping level (**Table ST3**), signifying enhanced electron mobility and interfacial conductivity. This trend is particularly evident for intermediate ZSS compositions (e.g., ZSS(0.15) - (0.20)), where minimized charge transfer resistance suggests a synergistic balance between defect engineering and lattice conductivity. These findings are consistent with the PL spectra, which show reduced photoluminescence intensity for the same compositions, indicating suppressed radiative recombination and more efficient separation of charge carriers.

2.2.4. Photocurrent

The transient photocurrent measurements (**Figure 3d**, ZIVE SP1, WonATech, Korea, with a standard three-electrode system) further substantiate the charge separation and transport dynamics of the ZSS nanostructures under light irradiation. Upon periodic light on/off cycles (SOLIS-1C, Thorlabs, USA), a sharp rise and decay in photocurrent density were observed, with intensity varying across the compositional series. Pure ZnS showed minimal response (~0.05 $\mu A/cm^2$), attributed to its wide bandgap and inefficient charge separation, while Ag_2S exhibited a moderate signal (~0.18 $\mu A/cm^2$) due to its narrower bandgap yet higher recombination. Remarkably, the ZSS nanoflowers, especially ZSS(0.15)

and ZSS(0.20), displayed significantly enhanced photocurrent responses of ~0.38 μA/cm^2 and ~0.35 μA/cm^2, respectively, indicating superior photoinduced charge generation and extended carrier lifetimes. These trends are well-supported by EIS measurements, where the charge transfer resistance (R_{ct}) for ZSS(0.15) and ZSS(0.20) was the lowest (~820 and ~860 Ω·cm^2, respectively), in contrast to ZnS (~6800 Ω·cm^2) and Ag_2S (~5100 Ω·cm^2), reflecting more efficient interfacial charge transport. Concurrently, these samples also exhibited suppressed PL intensity, compared to ZnS and Ag_2S, confirming reduced radiative recombination. Collectively, the synergy between high photocurrent response, low R_{ct}, and quenched PL intensity highlights the optimized charge carrier behavior achieved through optimal Zn substitution, ultimately promoting efficient ROS generation and photothermal conversion, both critical to enhancing therapeutic performance in PDT and PTT.

2.2.5. XPS

To investigate the electronic structure of the prepared materials, high-resolution XPS spectra (Omicron XPS, Scienta Omicron, Germany) were acquired for pristine Ag_2S and ZSS(0.15) nanostructures. The Ag 3d region of Ag_2S (**Figure 3e**) reveals two strong peaks located at 367.3 eV and 373.4 eV, assigned to Ag $3d_{5/2}$ and Ag $3d_{3/2}$, respectively. These binding energies are consistent with Ag^+ in Ag_2S [30]. Upon incorporation of Zn into the lattice, the Ag 3d peaks in ZSS(0.15) exhibit a slight positive shift to 367.5 eV and 373.6 eV. This upward shift in binding energy indicates a slight increase in the effective nuclear charge experienced by the Ag atoms, which can be attributed to electronic interactions and lattice distortion induced by Zn substitution. The shift reflects a partial withdrawal of electron density from the Ag atoms, likely resulting from charge redistribution between Zn^{2+} and Ag^+ species in the lattice. The S 2p core-level spectra (**Figure 3f**) further support this electronic modulation. In Ag_2S, the doublet peaks appear at 160.3 eV (S $2p_{3/2}$) and 161.7 eV (S $2p_{1/2}$), corresponding to divalent sulfide (S^{2-}) ions. For ZSS(0.15), the S 2p peaks are shifted slightly to higher binding energies, located at 160.73 eV and 161.91 eV, respectively. This subtle shift implies that the sulfur atoms experience a modified chemical environment due to neighboring Zn dopants, which may cause local lattice strain and altered electronic density around sulfur atoms. Such a shift also supports the hypothesis of a strong interaction between Zn and the Ag_2S matrix, rather than mere physical mixing. The Zn 2p spectrum (**Figure 3g**) of ZSS(0.15) displays well-defined peaks at 1021.9 eV (Zn $2p_{3/2}$) and 1044.9 eV (Zn $2p_{1/2}$), characteristic of Zn^{2+} species in a sulfide matrix [31]. The absence of any satellite peaks rules

out the presence of metallic Zn or ZnO impurities, confirming that Zn is successfully incorporated into the Ag_2S framework via cationic substitution rather than surface adsorption. This substitution is further validated by the consistent energy separation (~23 eV) between Zn $2p_{3/2}$ and Zn $2p_{1/2}$ peaks, indicative of spin–orbit coupling typical of divalent Zn in a tetrahedral coordination [32].

2.3. Photothermal and Photodynamic Performance

2.3.1. Photothermal activity

To evaluate the photothermal response of the synthesized ZSS nanostructures, temperature elevation studies were performed under continuous 660 nm laser irradiation (0.5 W/cm^2, 5 mm spot; Techhood (660 nm) word-line laser module, 300 mW max power, HK). The temperature change (ΔT) of various samples, including pristine Ag_2S and ZSS nanostructures was monitored over a 12-minute irradiation period. As shown in **Figure 3h**, all materials exhibited a gradual increase in temperature (Ebro TFI 54 Infrared Thermometer) over time, but with significantly varying efficiencies depending on the Zn substitution level. Among all tested compositions, the ZSS(0.15) sample demonstrated the most pronounced photothermal response, with a maximum ΔT of 30 °C, whereas the pristine Ag_2S exhibited only a ΔT of ~22 °C under identical conditions. The enhancement in photothermal performance upon Zn incorporation can be attributed to synergistic improvements in light absorption and non-radiative relaxation pathways introduced by Zn-mediated band structure modulation [33]. To gain further insights, heating and cooling profiles of ZSS(0.15) were recorded (**Figure SF2**), wherein the sample temperature rose from ambient (~25 °C) to a plateau of 55 °C within 12 minutes and returned close to the baseline after stopping irradiation. From the cooling profile, the photothermal conversion efficiency (η) was calculated to be 67.26%, indicating excellent light-to-heat conversion properties. Collectively, these observations suggest that Zn incorporation at 0.15 induces optimal defect states and band alignment, which not only improve charge separation and transport but also enhance non-radiative recombination routes, crucial for photothermal conversion [34]. The improved light-harvesting ability and reduced electron-hole recombination rates likely contribute to the higher photothermal output of ZSS(0.15), making it the most efficient composition for further photodynamic investigations.

2.3.2. ROS specific assays - DCFH-DA fluorescence

The generation of intracellular ROS under 660 nm laser irradiation (0.5 W/cm^2, 5 mm spot) was quantitatively monitored using the DCFH-DA fluorescence assay (**Figure 3i**). The fluorescence intensity increased progressively with irradiation time, confirming successful ROS generation across all tested compositions of ZSS nanostructures. Notably, ZSS(0.15) exhibited the highest fluorescence intensity at all time intervals, reaching ~1038 a.u. at 720 s, significantly surpassing Ag_2S, ZnS and all other Zn concentrations. The ranking of ROS generation efficiency followed the order: ZSS(0.15) > ZSS(0.20) > ZSS(0.10) > ZSS(0.25) > ZSS(0.05) > ZSS(0.00) > ZnS. These results correlate well with previous photocurrent and EIS data, where ZSS(0.15) exhibited the highest charge separation efficiency and lowest interfacial resistance, a favorable condition for ROS formation. Additionally, its lowest PL intensity confirms minimal recombination losses, allowing more charge carriers to participate in ROS-generating reactions. Overall, the combined findings from ROS, photothermal, PL, and electrochemical assays identify ZSS(0.15) as the most effective formulation, offering a balanced and enhanced dual-mode (photothermal and photodynamic) therapeutic potential.

2.4. In-vitro study

2.4.1. MTT-assay

To evaluate the phototherapeutic efficacy of the synthesized ZSS nanostructures, an MTT assay was conducted against MCF-7 breast cancer cells under both light irradiation (660 nm, 0.5 W cm^{-2}, 5 mm spot, 10 min) and dark conditions, across a concentration range of 0-25 μg/mL. All samples were compared with clinically used anticancer drug cisplatin as a control. Upon laser exposure (**Figure 4a**), all ZSS samples exhibited a clear dose-dependent cytotoxic response. Notably, ZSS(0.15) consistently outperformed the other compositions, showing significantly enhanced cell-killing efficiency. At a concentration of 25 μg/mL, ZSS(0.15) reduced the cell viability to ~12%, compared to 22% for ZSS(0.10), 30% for ZSS(0.05), and 38% for pristine Ag_2S. ZnS, lacking significant visible light absorption or charge separation ability, maintained high viability (~84%), serving as a negative reference. This enhanced activity is attributed to the synergistic photothermal (PTT) and photodynamic (PDT) mechanisms of ZSS nanostructures. The optimal Zn doping (0.15 molar ratio) likely promotes superior light absorption, efficient electron-hole separation, and intensified ROS generation consistent with the previously discussed results from photothermal measurements, photocurrent response, and ROS activity assay. In the absence of light (**Figure 4b**), all nanostructures displayed markedly lower cytotoxicity, with cell viability remaining above

75% even at the highest dose (25 μg/mL). For ZSS(0.15), cell viability was ~78%, affirming its low dark toxicity and strong photo-responsiveness indicating that the therapeutic effect is primarily light-triggered, confirming the biocompatibility of the system in non-irradiated conditions. Cisplatin, a well-established chemotherapeutic agent, showed robust cytotoxicity with an IC_{50} of ~10 μg/mL, reducing cell viability to ~9.1% at 25 μg/mL (**Figure 4c**). Interestingly, ZSS(0.15) closely matched this performance under laser irradiation, achieving an IC_{50} at ~15 μg/mL, highlighting its potential as an effective alternative. Based on these findings, it can be concluded that the ZSS nanostructures demonstrate excellent photodynamic and photothermal therapy (PDT/PTT) capabilities, with ZSS(0.15) emerging as the most promising composition. Therefore, ZSS(0.15) at 15 μg/mL (IC_{50}) was selected as the optimal concentration for all subsequent *in-vitro* biological experiments.

2.4.2. Cell staining & FACS

To further validate the cytotoxic effects observed in the MTT assay, nuclear integrity and intracellular ROS generation were assessed through DAPI and DHE staining, respectively (**Figure 4d-f**), while apoptotic progression was quantified using flow cytometry (FACS). As shown in the DAPI images, all treatment groups exhibited uniform nuclear morphology; however, the ZSS(0.15)+660 nm and Cisplatin groups showed signs of nuclear condensation and shrinkage, indicative of apoptotic changes [35]. DHE staining revealed minimal ROS presence in the control group, while a dramatic increase in red fluorescence intensity was observed in ZSS(0.15)+660 nm treated cells, suggesting robust intracellular ROS generation upon light irradiation. This confirms the effective photodynamic functionality of the ZSS(0.15) nanostructures. The ROS levels in the Cisplatin group were comparatively lower than ZSS(0.15)+660 nm, further underscoring the superior oxidative stress induced by the photodynamic/photothermal therapy. Flow cytometry analysis provided quantitative insights into cell fate. The control group showed a predominance of live cells (95.8%) with negligible apoptosis (3.6%) and death (0.6%). In contrast, the ZSS(0.15)+660 nm group exhibited a significant increase in apoptotic (8.0%) and dead (62.4%) populations, with live cells reduced to 24.8%. Notably, this cell death rate was substantially higher than that of the Cisplatin group, which showed 31.5% dead and 10.1% apoptotic cells, indicating the enhanced therapeutic efficacy of the ZSS(0.15)+660 nm. Collectively, these *in-vitro* results confirm that ZSS(0.15) under 660 nm irradiation induces substantial ROS-mediated cytotoxicity and apoptosis, in line with the MTT findings [36]. The

elevated ROS levels and apoptotic cell fractions support the proposed photodynamic therapeutic mechanism and warrant further exploration into associated apoptotic gene expression profiles [36].

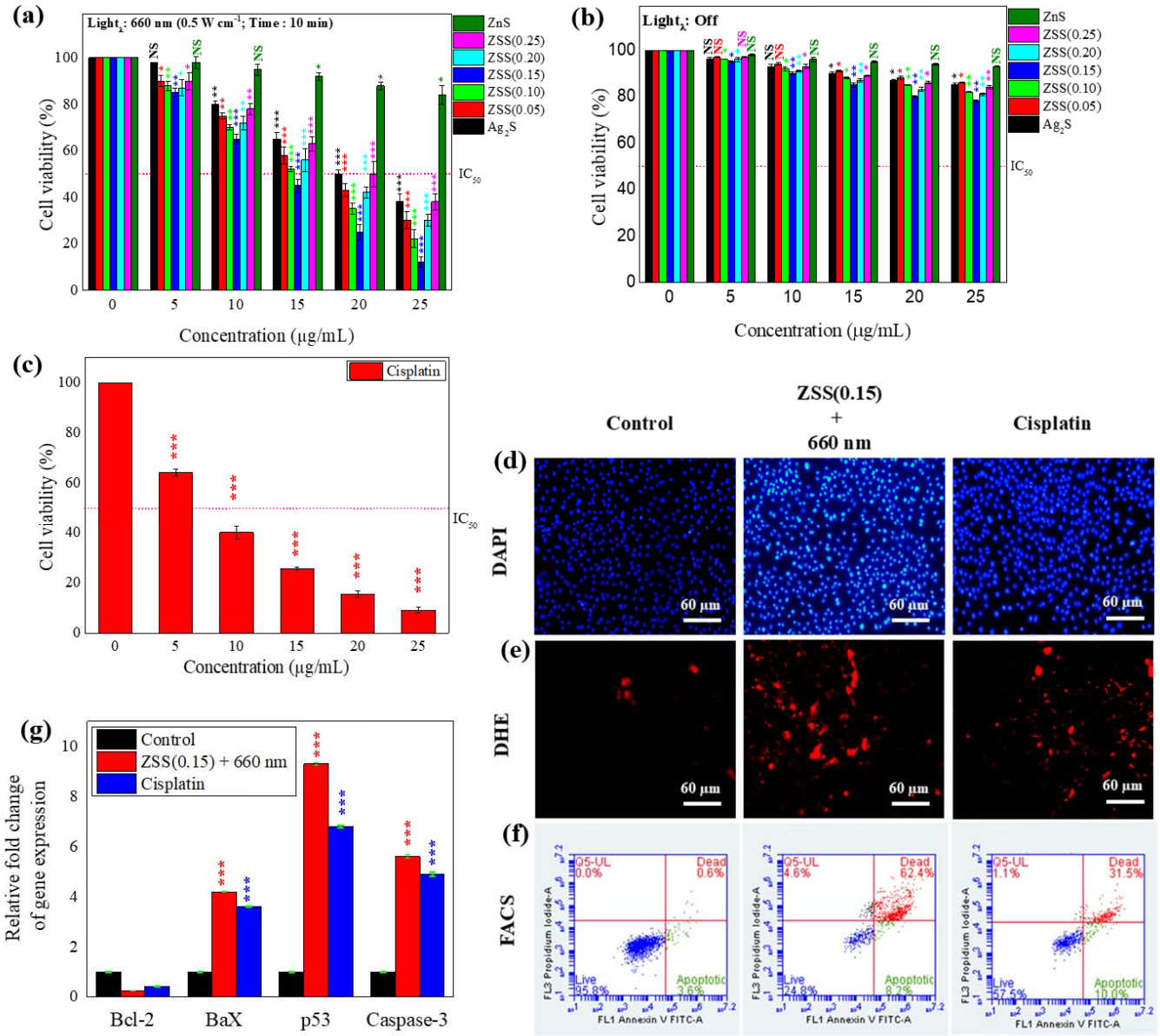

Figure 4 **(a)** Cell viability (MTT assay) under combined photothermal and photodynamic treatment (PTT/PDT); **(b)** Cell viability under dark conditions; **(c)** Cytotoxic effect of cisplatin; [Asterisks indicate statistically significant differences from 0 μg/mL within each treatment group; NS = no significance; * = $p < 0.05$; ** = $p < 0.01$; *** = $p < 0.001$] **(d)** DAPI staining for nuclear morphology; **(e)** DHE staining for intracellular ROS generation; **(f)** Flow cytometry (FACS) plots for apoptotic profiling; **(g)** Relative gene expression level [Asterisks indicate statistically

significant differences from control within each group; NS = no significance; * = $p < 0.05$; ** = $p < 0.01$; *** = $p < 0.001$].

2.4.3. Gene expression

To gain deeper insights into the molecular mechanism underlying the observed anticancer efficacy of the nanostructured system, the expression profiles of key apoptosis-related genes BCL2, BAX, P53, and CASP3, were evaluated in MCF-7 cells following treatment with ZSS(0.15) under 660 nm irradiation (15 μg/mL) and compared with cisplatin (10 μg/mL), both at their respective IC concentrations. As shown in **Figure 4g**, treatment with ZSS(0.15)+laser resulted in a marked downregulation of BCL2 (0.25-fold), a key anti-apoptotic gene [37, 38]. This reduction was significantly greater than that observed with cisplatin (0.42-fold), indicating a stronger inhibition of pro-survival signaling. Simultaneously, the pro-apoptotic genes were dramatically upregulated in response to ZSS(0.15). Specifically, BAX increased to 4.2-fold, P53 to 9.3-fold, and CASP3 to 5.6-fold, compared to respective fold increases of 3.6, 6.8, and 4.9 in cisplatin-treated cells. These data indicate that ZSS(0.15) activated the intrinsic apoptotic pathway more effectively than cisplatin, with a strong emphasis on mitochondrial dysfunction and P53-mediated transcriptional activity. The robust upregulation of P53, a central regulator of cellular stress responses, further suggests that oxidative stress generated via ROS played a major role in initiating apoptosis [39]. This is consistent with the earlier DCFH-DA fluorescence results, where ZSS(0.15) produced the highest ROS levels, and with the photothermal data, where ZSS(0.15) showed the most efficient photothermal conversion. The enhanced efficacy of ZSS(0.15) over cisplatin highlights its potential as a non-invasive, laser-triggered alternative with lower systemic toxicity and higher selectivity toward cancer cells [40].

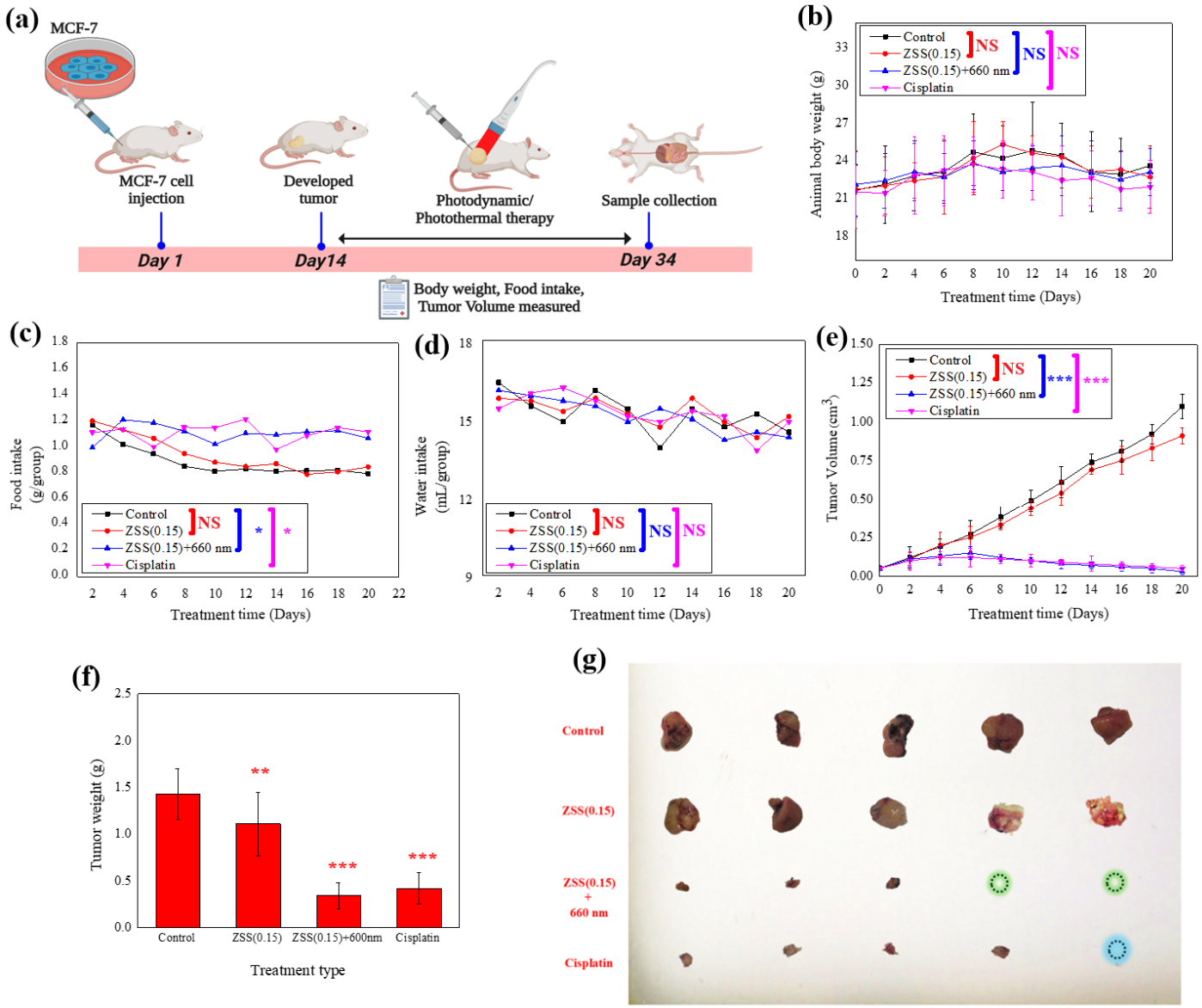
(a)
MCF-7
MCF-7 cell injection
Developed tumor
Photodynamic/ Photothermal therapy
Sample collection
Day 1
Day14
Day 34
Body weight, Food intake, Tumor Volume measured
(b)
Animal body weight (g)
Treatment time (Days)
Control
ZSS(0.15)
ZSS(0.15)+660 nm
Cisplatin
NS
(c)
Food intake (g/group)
Treatment time (Days)
(d)
Water intake (mL/group)
Treatment time (Days)
(e)
Tumor Volume (cm3)
Treatment time (Days)
***
(f)
Tumor weight (g)
Control
ZSS(0.15)
ZSS(0.15)+600nm
Cisplatin
Treatment type
**
***
(g)
Control
ZSS(0.15)
ZSS(0.15) + 660 nm
Cisplatin

Figure 5 (a) Schematic timeline of animal treatment; **(b)** Body weight changes; **(c)** Daily food intake; **(d)** Daily water intake; **(e)** Tumor volume progression in different treatment groups; **(f)** Final tumor weight; **(g)** Representative images of excised tumors post-treatment. [Asterisks indicate statistically significant differences from control group; NS = no significance; * = $p < 0.05$; ** = $p < 0.01$; *** = $p < 0.001$].

2.5. In-vivo Therapeutic Efficacy

2.5.1. Animal model: Setup and treatment

To investigate the *in-vivo* phototherapeutic application, C57BL/6J mice (6 weeks old) were subcutaneously inoculated with MCF-7 tumor xenografts. Following tumor establishment (14 days post-injection; defined as Day 0 of treatment; **Figure 5a**), the mice were randomized into four groups (n=5): Group I - Control; Group II - ZSS(0.15) (15 μg/mL, intratumoral); Group III - ZSS(0.15) (15 μg/mL, intratumoral) +660 nm laser irradiation (0.5 W/cm^2, 10 min, every 2 days); Group IV - Cisplatin (10 μg/mL, intraperitoneal). Body weight (**Figure 5b**) in the control group increased steadily from 21.64 g (Day 0) to 23.6 g (Day 20), while ZSS(0.15)-treated mice showed a comparable rise from 21.7 g to 22.7 g. Notably, the ZSS(0.15)+660 nm group maintained stable weights (22.1 g to 23.1 g), indicating minimal systemic burden, unlike the cisplatin group, which showed a slight decline (21.5 g to 21.9 g), suggesting mild toxicity. Food intake (**Figure 5c**) further supported these observations: ZSS(0.15)+laser-treated mice consumed between 0.997-1.211 g/day, slightly higher than control (0.797-1.168 g/day), while cisplatin group showed a progressive decline after Day 10, dropping to 0.982-1.002 g/day, indicative of treatment-associated distress. Similarly, water consumption (**Figure 5d**) in the ZSS(0.15)+laser group remained stable (16.1 to 14.3 mL), comparable to controls (16.4 to 14.5 mL), while cisplatin-treated mice exhibited a gradual decrease from 15.4 to 14.9 mL. In summary, these physiological metrics with stable body weight, sustained food and water intake, and absence of acute adverse effects strongly support the excellent biocompatibility of ZSS(0.15). More importantly, when irradiated with 660 nm irradiation, ZSS(0.15) maintained this biosafety profile, even while delivering potent photothermal and photodynamic tumor ablation, as established in prior *in-vitro* analyses. In contrast, cisplatin, although effective, exerted measurable systemic stress, evident from reduced food consumption and stagnant weight.

2.5.2. Tumor Suppression Efficacy and Visual Evidence

To evaluate the therapeutic efficacy of ZSS(0.15) *in-vivo*, tumor-bearing mice were treated over a 20-day period, and tumor progression was closely monitored. The control group exhibited rapid tumor growth (**Figure 5e**), with volumes escalating from 0.05 cm^3 on Day 0 to 1.10 cm^3 by Day 20, while the ZSS(0.15) - only group showed moderate suppression, reaching 0.91 cm^3. Notably, the ZSS(0.15)+660 nm light-treated group demonstrated a dramatic reduction in tumor volume, declining to just 0.03 cm^3 by Day 20, outperforming even the cisplatin group, which ended at 0.05 cm^3. Tumor weight measurements (**Figure 5f**) corroborated these findings, ZSS(0.15)+light resulted in a significantly reduced tumor mass (0.34 ± 0.14 g), closely followed by cisplatin (0.42 ± 0.17 g), while ZSS(0.15) alone and control groups maintained higher tumor burdens of 1.11 ± 0.34 g and 1.43 ± 0.27 g, respectively. Representative tumor images (**Figure 5g**) revealed complete tumor ablation in 2 out of 5 mice in the ZSS(0.15)+660 nm group, and in 1 out of 5 mice in the cisplatin group, visually substantiating the quantitative findings. This superior tumor inhibition under light irradiation is directly linked to the photothermal and photodynamic potency of ZSS(0.15), as previously evidenced by its highest photothermal conversion efficiency and ROS generation capability, validated via photoluminescence quenching and electron paramagnetic resonance (EPR) signals. Furthermore, enhanced charge separation and transfer properties observed through photocurrent and EIS studies suggest that ZSS(0.15) facilitates efficient electron–hole pair separation, crucial for ROS-mediated apoptosis [41]. The synergy of these properties culminates in profound tumor cell apoptosis and necrosis *in-vivo*. Collectively, these results firmly establish ZSS(0.15)+660 nm as a highly effective and biocompatible candidate for dual-modal photothermal and photodynamic cancer therapy [42], demonstrating tumor inhibition comparable to or even exceeding that of conventional chemotherapy, but with fewer systemic side effects.

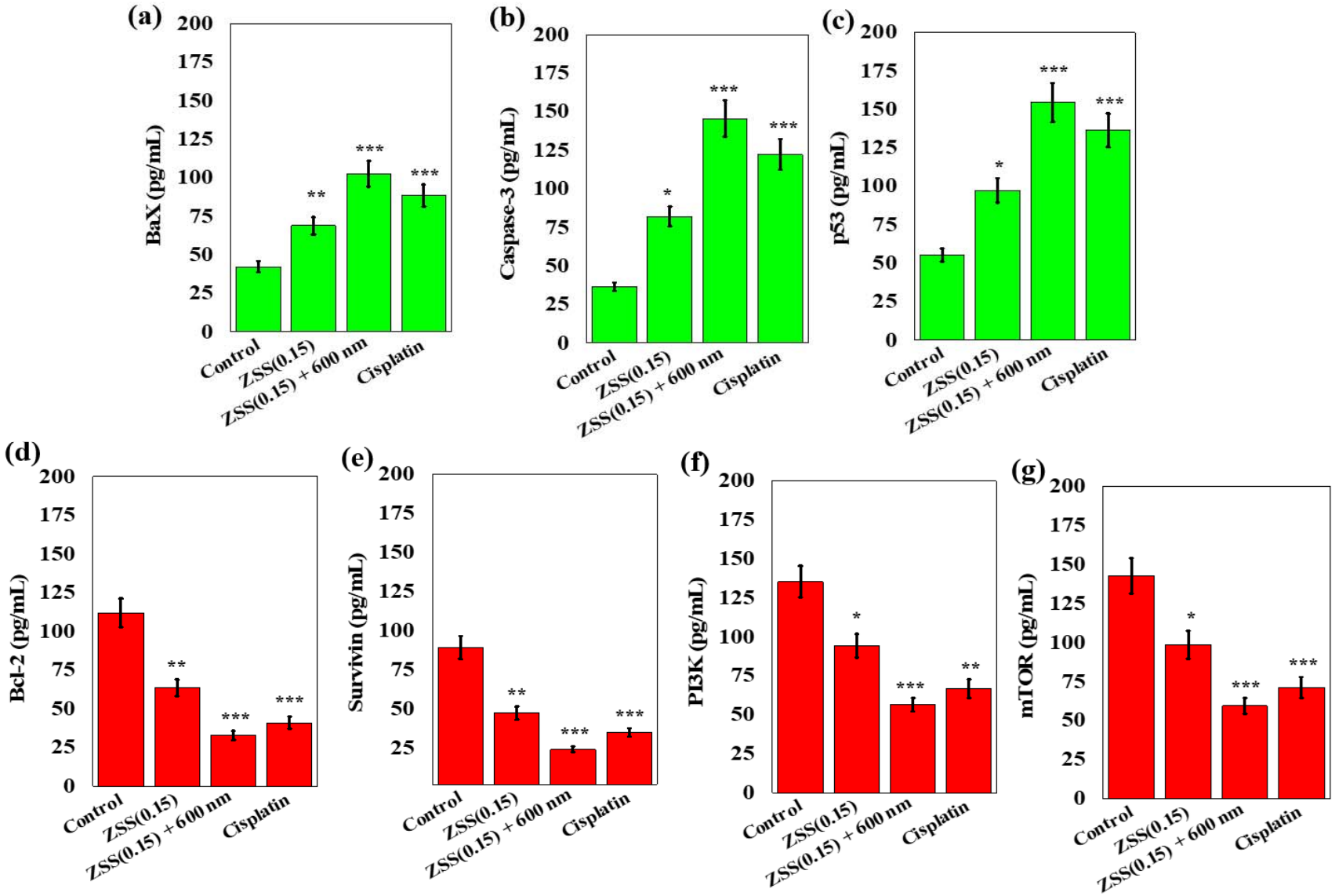
(a)
BaX (pg/mL)
200
175
150
125
100
75
50
25
0
**
***
***
Control
ZSS(0.15)
ZSS(0.15) + 600 nm
Cisplatin
(b)
Caspase-3 (pg/mL)
*
***
***
(c)
p53 (pg/mL)
*
***
***
(d)
Bcl-2 (pg/mL)
**
***
***
(e)
Survivin (pg/mL)
**
***
***
(f)
PI3K (pg/mL)
*
***
**
(g)
mTOR (pg/mL)
*
***
***

Figure 6 Protein quantification of apoptosis-related markers in tumor tissue homogenates using ELISA: **(a)** Bax, **(b)** Caspase-3, **(c)** p53, **(d)** Bcl-2, **(e)** Survivin, **(f)** PI3K, and **(g)** mTOR. [Asterisks indicate statistically significant differences from control group; NS = no significance; * = $p < 0.05$; ** = $p < 0.01$; *** = $p < 0.001$].

2.5.3. *Elisa*- Apoptotic marker (Pro/Anti) - Protein quantification

To further validate the apoptosis-inducing capabilities of ZSS(0.15), with and without 660 nm irradiation, the expression of key pro-apoptotic (Bax, Caspase-3, p53) and anti-apoptotic (Bcl-2, Survivin, PI3K, mTOR) proteins was quantified using ELISA in homogenized tumor tissues (**Figure 6**). The results revealed a significant upregulation of pro-apoptotic proteins (green bars) in the treatment groups, particularly in ZSS(0.15)+660 nm. Specifically, Bax expression rose from 42.3 ± 3.4 pg/mg in the control group to 68.9 ± 5.7 pg/mg in ZSS(0.15) and further to 102.6 ± 8.4 pg/mg in the ZSS(0.15)+660 nm group. Similarly, Caspase-3 levels increased from 36.5 ± 2.7 to 82.1 ± 6.4 and peaked at 145.5 ± 11.7 pg/mg. The tumor suppressor p53 [43] also followed this trend, increasing from 55.2 ± 4.3 to 97.3 ± 7.9 and then to 154.3 ± 12.6 pg/mg across the same groups. In contrast, anti-apoptotic proteins (red bars) were markedly suppressed in the treatment groups, most notably in the ZSS(0.15)+660 nm condition. Bcl-2 levels dropped from 111.9 ± 9.2 pg/mg in control to 63.6 ± 5.3 in ZSS(0.15) and down to 32.8 ± 2.9 in the irradiated group. Survivin, another potent anti-apoptotic marker [44], decreased from 89.4 ± 7.2 to 47.5 ± 4.2 and further to 24.2 ± 1.8 pg/mg, while PI3K and mTOR levels also exhibited a similar decline from 135.2 ± 10.1 and 142.7 ± 11.3 in the control group to 56.4 ± 4.3 and 59.3 ± 5.1 pg/mg, respectively, in the ZSS(0.15)+660 nm group. Comparatively, the cisplatin group showed intermediate responses, with pro-apoptotic markers elevated (e.g., Caspase-3: 122.3 ± 9.8 pg/mg) and anti-apoptotic markers downregulated (e.g., Bcl-2: 40.9 ± 3.9 pg/mg), albeit less effectively than the laser-activated nanomaterial. These findings confirm that the phototherapeutic activation of ZSS(0.15) not only enhances apoptotic signaling but also robustly inhibits survival pathways, suggesting a dual mechanism involving mitochondrial-mediated apoptosis and PI3K/mTOR pathway suppression [45]. This is consistent with earlier photothermal and ROS studies showing high local hyperthermia and reactive oxygen generation under 660 nm irradiation. Together, these results strongly support the forthcoming mechanistic insights, emphasizing ZSS(0.15)+660

nm as a potent nano-therapeutic platform that disrupts tumor homeostasis at both the protein and signaling cascade levels.

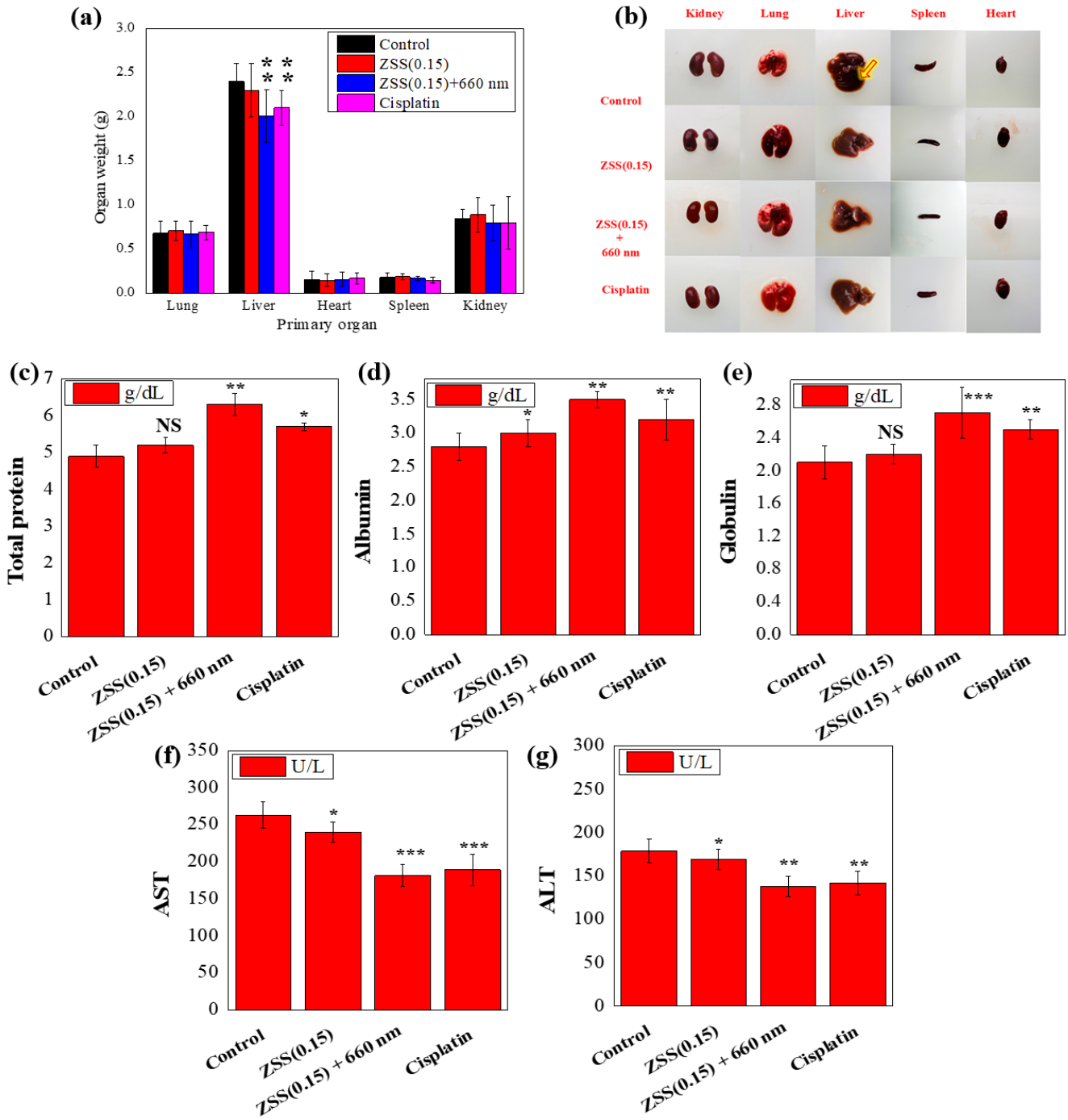

Figure 7 **(a)** Weights of primary organs and **(b)** their representative photographs; Liver function indicators measured by biochemical assays: **(c)** Total protein, **(d)** Albumin, **(e)** Globulin, **(f)** AST, and **(g)** ALT. [Asterisks indicate statistically significant

differences from control group; NS = no significance; * = $p < 0.05$; ** = $p < 0.01$; *** = $p < 0.001$].

2.6. In-vivo Biosafety Evaluation

2.6.1. Primary organ weight

To assess the systemic biosafety of ZSS(0.15)-based therapy, the primary organs: lung, liver, heart, spleen, and kidney were excised and weighed post-euthanasia (**Figure 7a**). Across all treatment groups, the organ weights remained largely comparable to the control group, indicating minimal systemic toxicity. Specifically, lung weights ranged from 0.67 ± 0.15 g in the ZSS(0.15)+660 nm group to 0.71 ± 0.11 g in the ZSS(0.15) group, closely matching the control (0.68 ± 0.14 g). Similarly, heart, spleen, and kidney weights showed only marginal fluctuations, with no statistically significant differences observed. For instance, kidney weights ranged from 0.80 ± 0.20 g to 0.89 ± 0.20 g, further supporting the absence of nephrotoxic effects. Notably, liver weight was slightly reduced in the ZSS(0.15)+660 nm group (2.01 ± 0.30 g) compared to control (2.40 ± 0.20 g), but this decrease was not accompanied by abnormal enlargement or discoloration typically indicative of hepatotoxicity. In fact, visual examination (**Figure 7b**) revealed a subtle bulge in the livers of control mice (yellow arrow), potentially reflecting inflammation or mild hepatic stress due to uncontrolled tumor progression, a phenomenon not observed in the treated cohorts. This visual anomaly reinforces the systemic burden imposed by untreated malignancy, whereas its absence in treated groups may signify reduced disease-associated organ strain [46]. Collectively, both quantitative and qualitative assessments suggest that ZSS(0.15), especially under 660 nm irradiation, does not elicit adverse organ-level toxicity, highlighting its promising safety profile as a therapeutic nanoplatform.

2.6.2. Liver functionality analysis

To further validate the hepatic biosafety of the ZSS(0.15)-based therapeutic system, a comprehensive liver functionality assessment was conducted by quantifying serum levels of total protein, albumin, globulin, AST, and ALT (**Figure 7c-g**). The control group, burdened by unchecked tumor progression, exhibited mildly compromised liver function, reflected by lower protein values (total protein: 4.9 ± 0.3 g/dL; albumin: 2.8 ± 0.2 g/dL) and elevated transaminases (AST: 263 ± 18 U/L; ALT: 179 ± 14 U/L), suggesting hepatic stress or inflammation, consistent with the subtle liver bulging observed (**Figure 7b**). In stark

contrast, the ZSS(0.15)+660 nm treated group demonstrated a markedly improved hepatic profile, with the highest levels of total protein (6.3 ± 0.3 g/dL), albumin (3.5 ± 0.12 g/dL), and globulin (2.7 ± 0.31 g/dL), coupled with significantly reduced AST (181 ± 15 U/L) and ALT (138 ± 12 U/L) levels, indicating robust liver function and minimal hepatic burden [47]. The standalone ZSS(0.15) and Cisplatin groups also showed moderate improvements over control but were inferior to the photodynamically enhanced ZSS(0.15)+660 nm treatment. These biochemical trends correlate well with the earlier primary organ weight data, where the liver in the ZSS(0.15)+660 nm group presented neither hypertrophy nor visible abnormalities, further reinforcing the biosafe nature of this nanoplatform. Thus, these findings not only dispel concerns of hepatic toxicity but also highlight the therapeutic efficiency of the ZSS(0.15)+660 nm system in mitigating systemic disease-induced organ stress, confirming its potential for safe clinical translation.

2.7. Mechanistic Insight

The therapeutic mechanism underlying the enhanced anticancer efficacy of ZSS(0.15) under 660 nm irradiation integrates both photothermal and photodynamic effects, synergistically promoting mitochondrial-mediated apoptosis in breast cancer cells. As depicted in the schematic (**Figure 8**), upon 660 nm light activation, ZSS(0.15) nanoflowers efficiently generate ROS alongside localized hyperthermia. These ROS act as a potent intracellular trigger, disrupting redox homeostasis and initiating mitochondrial dysfunction [48]. At the molecular level, ROS accumulation upregulates the tumor suppressor protein p53, which plays a pivotal role in promoting apoptosis. Elevated p53 expression facilitates the upregulation of the pro-apoptotic protein Bax while concurrently downregulating the anti-apoptotic protein Bcl-2, effectively tipping the balance toward cell death. This Bax/Bcl-2 modulation induces mitochondrial outer membrane permeabilization (MOMP), leading to the release of cytochrome c into the cytosol. Cytochrome c, once in the cytoplasm, binds to Apaf-1 and ATP to form the apoptosome, which subsequently activates initiator caspase-9 and executioner caspase-3 [49]. This cascade culminates in programmed cell death, as confirmed by significantly elevated caspase-3 levels in both *in-vitro* and *in-vivo* models treated with ZSS(0.15)+660 nm. Supporting the mechanistic cascade, *ELISA*-based protein quantification revealed markedly increased levels of Bax, Caspase-3, and p53, accompanied by strong suppression of anti-apoptotic markers such as Bcl-2 and Survivin. Moreover, key proliferative and survival-related signaling nodes: PI3K and mTOR, were significantly

downregulated, indicating effective inhibition of the PI3K/Akt/mTOR survival axis [50]. These mechanistic insights are reinforced by the *in-vivo* tumor regression data, apoptotic gene expression profiles, and excellent biosafety evidenced by normal organ weights, preserved hepatic function, and non-toxic histological observations. Altogether, these findings validate that the ZSS(0.15)+660 nm system not only induces efficient apoptotic cell death through a ROS-mediated mitochondrial pathway but also suppresses pro-survival signaling making it a promising candidate for precise and safe combinatorial cancer therapy.

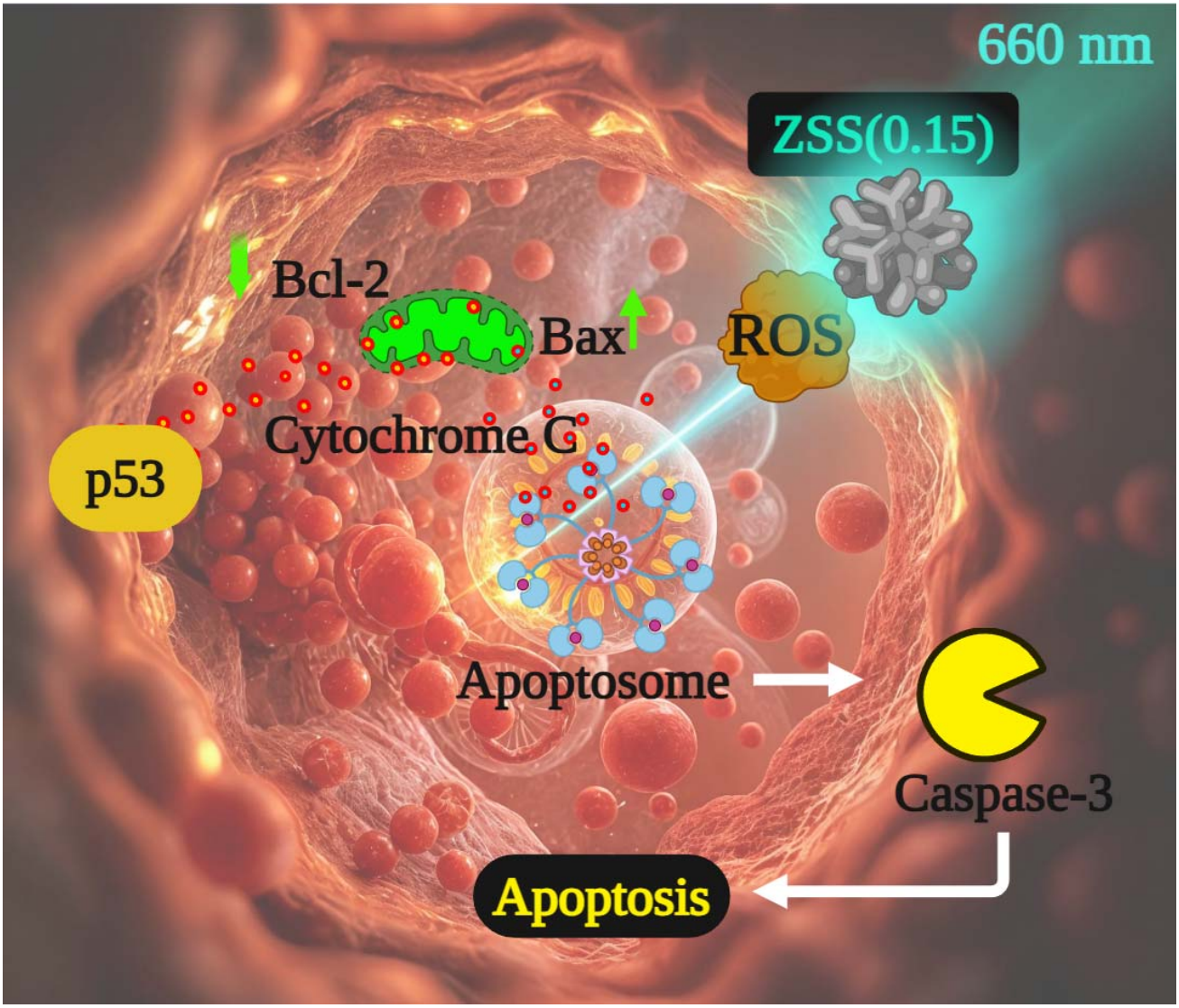

Figure 8 Proposed mechanism underlying the synergistic photothermal and photodynamic therapeutic effects of ZSS(0.15) against MCF-7 cells.

2.8. Broad-spectrum cytotoxicity of ZSS nanostructures across breast cancer subtypes

Breast cancer is a heterogeneous disease comprising molecularly distinct subtypes (luminal, HER2+, and triple-negative), each with different therapeutic vulnerabilities and resistance profiles [51]. Demonstrating efficacy across these subtypes is therefore critical for assessing the translational potential of new therapeutic platforms. Given the strong PTT/PDT effects of ZSS(0.15) against MCF-7 cells, we next evaluated its activity in triple-negative (MDA-MB-231), HER2+ (SK-BR-3), and luminal A (T47D) cells under identical conditions (660 nm, 0.5 W cm^{-2}, 10 min). As shown in **Figure 9a**, all three lines exhibited a pronounced, concentration-dependent decrease in viability, with IC_{50} values of 16.8 ± 0.9 μg/mL (MDA-MB-231), 15.6 ± 0.7 μg/mL (SK-BR-3), and 15.9 ± 0.8 μg/mL (T47D), indicating largely preserved potency across molecular subtypes. At the IC_{50} concentration for MCF-7 cells (15 μg/mL), SK-BR-3 and T47D showed viability close to 50%, whereas MDA-MB-231 retained ~60% viability (**Figure 9b**), consistent with the more aggressive and treatment-resistant phenotype typically associated with triple-negative breast cancers [52]. Importantly, these results highlight that Zn-doped Ag_2S nanostructures maintain high potency across ER+, HER2+, and triple-negative breast cancer contexts, with IC_{50} values in a clinically relevant range and substantially lower than those reported for several standard therapeutics [53-56]. The broad-spectrum efficacy further supports the notion that Zn-induced enhancements in photothermal conversion and ROS generation are subtype-independent, providing a versatile nanoplatform for diverse clinical settings.

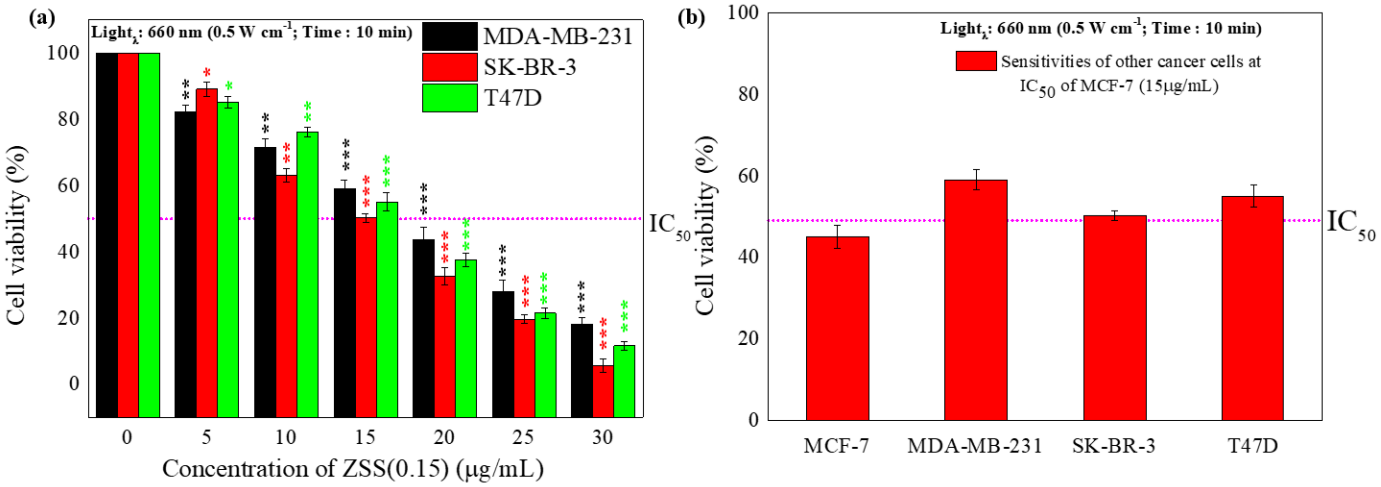

Figure 9 **(a)** Cell viability (MTT assay) under combined photothermal and photodynamic treatment (PTT/PDT) of ZSS(0.15) against other selected cancer cell lines [Asterisks indicate statistically significant differences from 0 µg/mL within each treatment group; NS = no significance; * = $p < 0.05$; ** = $p < 0.01$; *** = $p < 0.001$] **(b)** comparative plot of IC_{50} values for the select cancer cell lines.

3. CONCLUSION

In summary, we developed Zn-doped Ag_2S nanostructures (ZSS), with ZSS(0.15) identified as the most effective composition for light-triggered cancer therapy. Under 660 nm irradiation, this nanoplatform combined strong photothermal heating with efficient ROS generation, enabling synergistic therapeutic effects.

Key outcomes of this work include:

- **Enhanced therapeutic efficacy**: ZSS(0.15) achieved nearly 97% tumor suppression *in-vivo* with no systemic toxicity.
- **Mechanistic insight**: Zn doping favored improved charge separation and light utilization, boosting both photothermal and photodynamic activity.
- **Safety advantage**: Compared to cisplatin, ZSS(0.15) showed minimal side effects while maintaining superior cancer cell killing.
- **Broad applicability**: Consistent performance was demonstrated across multiple breast cancer subtypes, not limited to a single model.

These findings highlight Zn doping as a powerful strategy to optimize Ag_2S-based nanoplatforms for dual-mode cancer therapy. While highly encouraging, further evaluation in orthotopic and metastatic tumor models, integration with targeted delivery systems, and exploration of deeper tissue-penetrating light sources will be critical for clinical translation. Taken together, our study positions ZSS(0.15) as a promising next-generation nanomedicine for safe, effective, and versatile photothermal–photodynamic breast cancer therapy.

4. EXPERIMENTAL

4.1. Materials

All reagents and chemicals employed in this study were purchased from Sigma-Aldrich (South Korea) and used without any further purification. Deionized water (DI water) was used in all procedures involving aqueous media.

4.2. Synthesis of $Zn_xAg_{2-2x}S$ (ZSS)nanostructures

The synthesis of $Zn_xAg_{2-2x}S$ nanostructures (ZSS) was accomplished via a two-step hydrothermal method involving a cation exchange strategy. Initially, pristine Ag_2S nanostructures were synthesized by dissolving silver nitrate ($AgNO_3$, 0.02 M) in 50 mL of deionized water and stirring at 25 °C for 30 minutes at 600 rpm. A freshly prepared aqueous solution of sodium sulfide (Na_2S, 0.01 M, 50 mL) was then added dropwise under constant stirring (600 rpm), resulting in a black dispersion, which was stirred further for 6 hours at room temperature. The mixture was then transferred to a Teflon-lined autoclave and subjected to hydrothermal treatment at 150 °C for 16 hours. After natural cooling to room temperature, the Ag_2S product was collected, washed thoroughly with deionized water and ethanol, and subsequently dried. To obtain the ZSS nanostructures, the as-synthesized Ag_2S was redispersed in deionized water and treated with varying concentrations of zinc nitrate ($Zn(NO_3)_2$) solution to achieve controlled Ag^+/Zn^{2+} ion exchange. The molar ratios of $Ag^+:Zn^{2+}$ were adjusted as 1.95:0.05, 1.90:0.10, 1.85:0.15, 1.80:0.20, 1.75:0.25, and 1.70:0.30. The mixture was stirred at 25 °C for 30 minutes and then subjected to a second hydrothermal treatment at 150 °C for 16 hours to facilitate partial substitution of Ag^+ by Zn^{2+} within the Ag_2S lattice. The resulting $Zn_xAg_{2-2x}S$ nanostructures were washed with deionized water and ethanol, followed by freeze-drying. For comparison, pure ZnS nanostructures were synthesized under identical hydrothermal conditions by replacing $AgNO_3$ with $Zn(NO_3)_2$ (**Figure 1a**).

4.3. In-vitro studies

4.3.1. Cell culture

The MCF-7 human breast adenocarcinoma cell line (ATCC HTB-22, RRID: CVCL_0031) was obtained from the American Type Culture Collection (ATCC, Manassas, VA, USA). Cells were maintained in Dulbecco's Modified Eagle Medium (DMEM), supplemented with 10% fetal bovine serum (FBS) and 1% penicillin-streptomycin solution. Cultures were incubated at 37 °C in a humidified atmosphere containing 5% CO_2. All cell handling procedures were carried out under aseptic conditions. Once the cultures reached approximately 80% confluence, cells were passaged. For experimental treatments, cells were

seeded at a density of 5×10^2 cells/cm^2 and allowed to adhere for 4 hours before the application of test formulations.

4.3.2. MTT assay

MCF-7 cells were seeded into 96-well plates at a density of 1×10^5 cells per well and incubated for 24 hours to allow for attachment. After incubation, the culture medium was replaced with 100 μL of fresh DMEM containing various concentrations of the synthesized nanostructures (5, 10, 15, 20, and 25 μg/mL). For PDT evaluation, cells were exposed to a 660 nm laser at an intensity of 0.5 W/cm^2 for 10 minutes, followed by incubation for an additional 24 hours. The cells in control groups were kept in the dark under identical conditions. Subsequently, 10 μL of MTT solution (5 mg/mL in PBS) was added to each well, and the plates were incubated for 4 hours at 37 °C to allow the formation of formazan crystals. The medium was then carefully removed, and 100 μL of dimethyl sulfoxide (DMSO) was added to solubilize the crystals. Absorbance was measured at 570 nm using a microplate reader (Infinite M1000 Pro, Tecan, Switzerland). Untreated cells were used as the negative control, while cells treated with cisplatin served as the positive control [57].

4.3.3. FACS

To evaluate apoptosis and necrosis induced by ZSS nanostructures, cells were stained with Annexin V-FITC and propidium iodide (PI) following the manufacturer's instructions. In brief, cells were seeded into 6-well plates at a density of 1×10^5 cells per well and incubated for 24 hours to facilitate attachment. After incubation, the growth medium was replaced with fresh medium containing ZSS nanostructures exposed to a 660-nm laser at an intensity of 0.5 W/cm^2 for 10 minutes. Following that 24-hour incubation, cells were harvested, rinsed twice with cold phosphate-buffered saline (PBS), and stained with Annexin V-FITC and PI. Staining was performed in the dark for 15 minutes at room temperature to minimize light-induced degradation. The stained cells were then analyzed by flow cytometry using a BD Accuri C6 cytometer to quantify the proportions of viable, early apoptotic, late apoptotic, and necrotic cells [58].

4.3.4. Fluorescent staining

Following 24-hour treatment with ZSS nanostructures, both adherent and floating MCF-7 cells were carefully collected and washed with ice-cold 1× PBS to remove residual medium and treatment agents. The cells were subsequently fixed with 1 mL of 4%

paraformaldehyde for 20 minutes at room temperature to maintain cellular morphology. After fixation, cells were rinsed again with PBS to eliminate any excess fixative. For assessment of nuclear integrity and oxidative stress, cells were stained with 4',6-diamidino-2-phenylindole (DAPI) to detect nuclear condensation and fragmentation, and with dihydroethidium (DHE) to visualize intracellular ROS, following the manufacturer's recommended protocols. Fluorescence imaging was performed using a Nikon Ti-E inverted fluorescence microscope equipped with appropriate excitation and emission filters for DAPI and DHE. High-resolution images were acquired at 10× magnification [58].

4.3.5. Gene expression analysis

Total RNA was isolated from MCF-7 cells treated with ZSS nanostructures and cisplatin using the TRIzol reagent, following the manufacturer's guidelines (Thermo Fisher Scientific, South Korea). For cDNA synthesis, 2 µg of RNA was used in a 40 µL reverse transcription reaction containing 1× RT buffer, 5 mM $MgCl_2$, 10 mM dithiothreitol (DTT), 5 µM oligo(dT) primers (15-18 bases), 1 mM dNTP mix, 1 U/µL RNase inhibitor, and 10 U/µL M-MLV reverse transcriptase. The reaction was initiated by heating at 70 °C for 10 minutes, followed by rapid cooling at 4 °C for 2 minutes, and then incubation at 37 °C for 60 minutes to complete the reverse transcription [59]. Quantification of gene expression was performed using SYBR Green-based quantitative real-time PCR (qRT-PCR) on a ViiA™ 7 Real-Time PCR system (Applied Biosystems). The expression levels of apoptosis-related genes, including BCL2, BAX, P53, and CASP3 were analyzed using primers obtained from TaKaRa (South Korea) (**Table ST2**). Relative gene expression was normalized against an internal control gene (GAPDH) and analyzed using the ΔΔCt method.

4.4. In-vivo studies

4.4.1. Animal care and Ethical Compliance

All experimental procedures involving animals were carried out in accordance with protocols approved by the Institutional Animal Care and Use Committee (IACUC) of Jeonbuk National University, Republic of Korea. For *in-vivo* evaluation of anticancer activity, 6 week-old female C57BL/6J mice (average body weight ~20 g) were obtained from Daehan BioLink (Eumsung, Korea). The mice were housed in a specific pathogen-free (SPF) facility under controlled experimental conditions, including a constant temperature of 23 ± 3 °C, regulated humidity, and a 12-hour light/dark cycle. Animals had free access to standard rodent feed and clean water throughout the duration of the experiment. All the *in-*

vivo experiments were conducted in compliance with ARRIVE guidelines to ensure scientific rigor and ethical standards.

4.4.2. Tumor induction

After a one-week acclimation period, mice were pre-implanted subcutaneously with 17β-estradiol pellets (0.72 mg (60 day release) Thermo Fisher Scientific, Cat: NC9032951) 72 hours prior to tumor inoculation to support the estrogen-dependent MCF-7 phenotype. MCF-7 cell suspension (1×10^5 cells) was suspended in a 1:1 mixture of cold PBS and Corning Matrigel® Matrix, High Concentration (HC)/LDEV-free (Cat: 354248) and injected subcutaneously into the dorsal flank of each mouse to establish localized xenografts. The estradiol supplementation-maintained ER activity, while the Matrigel depot stabilized the inoculum and enhanced local engraftment, ensuring reproducible and well-localized tumor formation. Tumor growth was systematically monitored at predefined intervals. Measurements of tumor length (A) and width (B) were taken using a digital vernier caliper. Tumor volume (V) was calculated using the standard ellipsoid formula: $\mathbf{V = A \times B^2 / 2}$. This calculation allowed for consistent and accurate tracking of tumor progression throughout the experimental period [60].

4.4.3. Animal treatment

When the tumors reached an approximate volume of 50 mm^3, the mice were randomly divided into four experimental groups (n = 5 per group). Treatments were administered over a period of 20 days, during which each mouse received tail vein injections of either cisplatin or ZSS nanostructure formulations at a dosage of 10 mg/kg body weight, which was determined based on preliminary toxicity screening and literature review. Injections were administered every two days. For the groups receiving photothermal therapy, near-infrared laser irradiation (660 nm, 0.5 W/cm^2, 10 min) was applied 24 hours after each injection to assess the combined therapeutic effect of the nanostructures and light exposure. Tumor dimensions were measured every two days using a vernier caliper, and tumor volume was calculated as previously described. Additionally, body weight, food intake, and water consumption were recorded to evaluate the general health and treatment response of the animals. At the end of the study, all mice were humanely euthanized using carbon dioxide asphyxiation. Tumors were excised, weighed, and preserved for further analyses. Major organs, including the kidneys, lungs, liver, spleen, and heart were also collected and weighed for subsequent assessments.

4.4.4. Elisa- Apoptotic marker (Pro/Anti) – Protein quantification

The tumor tissues excised from mice were homogenized in ice-cold phosphate buffered saline (PBS) using a tissue homogenizer to ensure complete cell lysis and release of intracellular proteins. The resulting homogenates were centrifuged at 2000 rpm for 15 minutes at 4 °C, and the clear supernatants were carefully collected for the subsequent quantification of apoptotic markers. Protein levels of both pro-apoptotic (Bax (Cat. No: MBS2513810), Caspase-3 (Cat. No: MBS260710), and p53 (Cat. No: MBS355295)) and anti-apoptotic ((Bcl-2 (Cat. No: MBS701787), Survivin (Cat. No: MBS030425), mTOR (Cat. No: MBS2505637), and PI3K (Cat.No: MBS268899)) proteins were determined using commercially available ELISA kits procured from MyBiosource (San Diego, CA, USA), following the manufacturer's guidelines. Briefly, 40 µL of sample diluent was added to each well designated for the tumor samples, while 50 µL of standard solution was added to the wells reserved for standard curve generation. Subsequently, 100 µL of horseradish peroxidase (HRP)-conjugated reagent was added to all wells, and the plate was incubated at 37 °C for 60 minutes to facilitate antigen–antibody binding. After incubation, the wells were washed five times with the provided wash buffer to remove unbound reagents. Thereafter, 50 µL each of Chromogen Solution A and Chromogen Solution B were added to every well, gently mixed, and incubated in the dark at 37 °C for 15 minutes to develop the color. The enzymatic reaction was terminated by the addition of 50 µL of stop solution, leading to a color change from blue to yellow. Absorbance was measured at 450 nm using a microplate reader, and the concentration of each apoptotic marker was calculated based on the standard curve derived from known reference concentrations [61, 62].

4.4.5. Liver functionality test

To assess liver function, the excised liver tissues were first homogenized in chilled PBS using a tissue homogenizer to ensure uniform sample processing. The resulting homogenates were centrifuged at 2000 rpm for 15 minutes at 4 °C to separate the supernatant, which was then collected for subsequent biochemical evaluation. Key hepatic function indicators, including total protein (Cat. No: MBS2540545), albumin (Cat. No: MBS730500), globulin (Cat. No: MBS2703040), alanine transaminase (ALT, Cat. No: MBS264333), and aspartate transaminase (AST, Cat. No: MBS450720), were measured using commercially available colorimetric assay kits (MyBiosource, San Diego, CA, USA).

All analyses were conducted in strict accordance with the manufacturers' protocols to maintain consistency and analytical accuracy [61, 63].

4.5. Broad-Spectrum Cytotoxicity Across Breast Cancer Subtypes

While MCF-7 cells were selected as the primary model to evaluate the mechanistic basis of ZSS-mediated photothermal and photodynamic effects, we further extended the investigation to additional breast cancer subtypes (MDA-MB-231; SK-BR-3; T47D) cells under identical conditions (ZSS(0.15, 660 nm, 0.5 W cm^{-2}, 10 min) to assess the broader applicability of the treatment.

4.6. Statistical analysis

All statistical analyses were conducted using SPSS software (version 22). Differences among multiple groups were assessed by one-way analysis of variance (ANOVA), followed by Tukey's post hoc test to determine specific group differences. p-value < 0.05 was considered statistically significant. All the results are presented as Average $\pm$ standard deviation (SD).

SUPPORTING INFORMATION

Supporting Information is available from the Wiley Online Library or from the author.

ACKNOWLEDGEMENTS

This work was supported by the National Research Foundation of Korea (NRF) grant funded by the Korea government, MSIT [RS-2025-00523589] and MOE [2020R1I1A3054429], and by research funds from Jeonbuk National University in 2023.

CONFLICTS OF INTEREST

The authors declare that they have no known competing financial interests or personal relationships that could have influenced the findings reported in this paper.

DATA AVAILABILITY

Relevant data can be made available on request.

REFERENCES

1. Kim, J.; Harper, A.; McCormack, V.; Sung, H.; Houssami, N.; Morgan, E.; Mutebi, M.; Garvey, G.; Soerjomataram, I.; Fidler-Benaoudia, M. M., *Nature Medicine* **2025**, 1-9.
2. Sonkin, D.; Thomas, A.; Teicher, B. A., *Cancer Genetics* **2024,** *286-287*, 18-24. DOI https://doi.org/10.1016/j.cancergen.2024.06.002.
3. Xiong, X.; Zheng, L.-W.; Ding, Y.; Chen, Y.-F.; Cai, Y.-W.; Wang, L.-P.; Huang, L.; Liu, C.-C.; Shao, Z.-M.; Yu, K.-D., *Signal Transduction and Targeted Therapy* **2025,** *10* (1), 49.
4. Nkune, N. W.; Abrahamse, H., *Journal of Biophotonics* **2025,** *n/a* (n/a), e70005. DOI https://doi.org/10.1002/jbio.70005.
5. Zhao, Z.; Chen, T.; Li, J.; Xue, X.; Ge, J.; Wang, P., *Smart Molecules* **2025,** *3* (2), e20240049. DOI https://doi.org/10.1002/smo.20240049.
6. Yang, F.; Chen, F.; Li, S.; Wang, S.; Peng, L.; Deng, S.; Zhang, F.; Jeschke, U.; Wang, Y.; Luo, C., *Chemical Engineering Journal* **2025,** *516*, 163962. DOI https://doi.org/10.1016/j.cej.2025.163962.
7. Papa, V.; Furci, F.; Minciullo, P. L.; Casciaro, M.; Allegra, A.; Gangemi, S. Photodynamic Therapy in Cancer: Insights into Cellular and Molecular Pathways *Current Issues in Molecular Biology* [Online], **2025**.
8. Jyothish, B.; Jacob, J., *Surfaces and Interfaces* **2025,** *56*, 105553. DOI https://doi.org/10.1016/j.surfin.2024.105553.
9. Hu, J.-J.; Chen, Y.; Lou, X.; Xia, F.; Wu, X.; Yoon, J., *Coordination Chemistry Reviews* **2025,** *532*, 216526. DOI https://doi.org/10.1016/j.ccr.2025.216526.
10. Oh, H. S.; Mohan, H.; Sathya, P. M.; Kim, G.; Ha, G. H.; Shin, T., *Materials Today Communications* **2023,** *34*, 105194.
11. Zhang, Y.; Zhang, Y.; Li, Y.; Fu, Y.; Zhao, Y.; Zhao, W.; Li, R.; Xian, Y.; Tu, K.; Wu, F.; Li, C.; Hou, Y.; Zhang, M., *Chemical Engineering Journal* **2023,** *474*, 145685. DOI https://doi.org/10.1016/j.cej.2023.145685.
12. Wang, J.; Huang, Z.; Wu, Y.; Jiang, X.; Ji, Y.; Braeckmans, K.; Wang, M.; Wang, L.; Chen, W. R.; Xia, Y.; Tang, Z.; Xu, X., *BMC Biology* **2025,** *23* (1), 111. DOI 10.1186/s12915-025-02215-w.
13. Lin, Y.; Han, D.; Li, Y.; Tan, L.; Liu, X.; Cui, Z.; Yang, X.; Li, Z.; Liang, Y.; Zhu, S.; Wu, S., *ACS Sustainable Chemistry & Engineering* **2019,** *7* (17), 14982-14990. DOI 10.1021/acssuschemeng.9b03287.

14. Zhu, K.; Li, Z.; Cao, J.; Cao, Y.; Wang, J.; Wang, S.; Chen, L.; Zhou, H.; Huang, W.; Zou, H.; Li, Q.; Mu, J.; Song, J., *Advanced Science* **2025,** *n/a* (n/a), 2417828. DOI https://doi.org/10.1002/advs.202417828.
15. Liu, T.; Zhang, X.; Liu, D.; Chen, B.; Ge, X.; Gao, S.; Song, J., *Advanced Optical Materials* **2021,** *9* (12), 2100233. DOI https://doi.org/10.1002/adom.202100233.
16. Tabrizi, N.; Jamali-Sheini, F.; Ebrahimiasl, S.; Cheraghizade, M., *Optical Materials* **2024,** *152*, 115374. DOI https://doi.org/10.1016/j.optmat.2024.115374.
17. Wang, C.; Zheng, H.; Ma, R.; Zheng, X.; Guan, X. Ag2S/Zn2+-Decorated g-C3N4 Type-II Heterojunction with Wide-Spectrum Response: Construction and Photocatalytic Performance in Ciprofloxacin Degradation *Molecules* [Online], **2025**.
18. Tang, Z.; Yang, H.; Sun, Z.; Zhang, Y.; Chen, G.; Wang, Q., *Nano Research* **2023,** *16* (10), 12315-12322. DOI 10.1007/s12274-023-5952-z.
19. Dai, X.; Cheng, H.; Bai, Z.; Li, J., *Journal of Cancer* **2017,** *8* (16), 3131.
20. Orrantia-Borunda, E.; Anchondo-Nuñez, P.; Acuña-Aguilar, L. E.; Gómez-Valles, F. O.; Ramírez-Valdespino, C. A., *Breast Cancer [Internet]* **2022**.
21. Mandari, K. K.; Im, Y.; Lee, Y.-A.; Pandey, S.; Kang, M., *Applied Surface Science* **2025,** *704*, 163452. DOI https://doi.org/10.1016/j.apsusc.2025.163452.
22. Patil, B. N., *Journal of Applied Spectroscopy* **2025,** *92* (1), 146-150. DOI 10.1007/s10812-025-01890-5.
23. Yin Win, K.; Feng, S.-S., *Biomaterials* **2005,** *26* (15), 2713-2722. DOI https://doi.org/10.1016/j.biomaterials.2004.07.050.
24. Feng, H.; Wang, J.; Fan, W.; Zhang, C., *Materials Letters* **2014,** *126*, 67-70. DOI https://doi.org/10.1016/j.matlet.2014.04.037.
25. Geravand, M.; Jamali-Sheini, F., *Advanced Powder Technology* **2019,** *30* (2), 347-358. DOI https://doi.org/10.1016/j.apt.2018.11.012.
26. Yang, Z.-C.; Gu, Q.-S.; Chao, J.-J.; Tan, F.-Y.; Mao, G.-J.; Hu, L.; Ouyang, J.; Li, C.-Y., *Analytica Chimica Acta* **2024,** *1316*, 342860. DOI https://doi.org/10.1016/j.aca.2024.342860.
27. Jagadeeswararao, M.; Swarnkar, A.; Markad, G. B.; Nag, A., *The Journal of Physical Chemistry C* **2016,** *120* (34), 19461-19469. DOI 10.1021/acs.jpcc.6b06394.
28. Zhang, Z.; Yan, H.; Qiu, B.; Ran, P.; Cao, W.; Jia, X.; Huang, K.; Li, X., *Small* **2022,** *18* (21), 2200813. DOI https://doi.org/10.1002/smll.202200813.

29. Guo, M.; Xing, Z.; Zhao, T.; Li, Z.; Yang, S.; Zhou, W., *Applied Catalysis B: Environmental* **2019,** *257*, 117913. DOI https://doi.org/10.1016/j.apcatb.2019.117913.
30. Chen, Q.; Yang, X.; Fu, X.; Pan, J.; Zhou, J.; Zhou, G.; Cheng, K., *Chemical Engineering Journal* **2024,** *499*, 156242. DOI https://doi.org/10.1016/j.cej.2024.156242.
31. Mohan, H.; Ramalingam, V.; Adithan, A.; Natesan, K.; Seralathan, K.-K.; Shin, T., *Journal of Hazardous Materials* **2021,** *416*, 126209.
32. Tiwari, N.; Gaikwad, P.; Kamat, R. K.; Kulkarni, S., *Nano Trends* **2025,** *10*, 100110. DOI https://doi.org/10.1016/j.nwnano.2025.100110.
33. Shou, P.; Yu, Z.; Wu, Y.; Feng, Q.; Zhou, B.; Xing, J.; Liu, C.; Tu, J.; Akakuru, O. U.; Ye, Z.; Zhang, X.; Lu, Z.; Zhang, L.; Wu, A., *Advanced Healthcare Materials* **2020,** *9* (1), 1900948. DOI https://doi.org/10.1002/adhm.201900948.
34. Vinícius-Araújo, M.; Shrivastava, N.; Sousa-Junior, A. A.; Mendanha, S. A.; Santana, R. C. D.; Bakuzis, A. F., *ACS Applied Nano Materials* **2021,** *4* (2), 2190-2210. DOI 10.1021/acsanm.1c00027.
35. Almuqbil, R. M., *Advances in Pharmacological and Pharmaceutical Sciences* **2024,** *2024* (1), 4646855. DOI https://doi.org/10.1155/2024/4646855.
36. Solanki, R.; Rajput, P. K.; Jodha, B.; Yadav, U. C. S.; Patel, S., *Scientific Reports* **2024,** *14* (1), 2595. DOI 10.1038/s41598-024-51970-3.
37. Kong, L.; Xing, L.; Zhou, B.; Du, L.; Shi, X., *ACS Applied Materials & Interfaces* **2017,** *9* (19), 15995-16005. DOI 10.1021/acsami.7b03371.
38. Li, D.; Zhang, Y.; Wen, S.; Song, Y.; Tang, Y.; Zhu, X.; Shen, M.; Mignani, S.; Majoral, J.-P.; Zhao, Q., *Journal of Materials Chemistry B* **2016,** *4* (23), 4216-4226.
39. Li, S.; Lui, K.-H.; Lau, W.-S.; Chen, J.; Lo, W.-S.; Li, X.; Gu, Y.-J.; Lin, L.-t.; Wong, W.-T., *ACS Applied Materials & Interfaces* **2022,** *14* (29), 33712-33725. DOI 10.1021/acsami.2c07592.
40. Qi, M.-H.; Wang, D.-D.; Qian, W.; Zhang, Z.-L.; Ao, Y.-W.; Li, J.-M.; Huang, S.-W., *Advanced Materials* **2025,** *37* (5), 2412191. DOI https://doi.org/10.1002/adma.202412191.
41. Qi, B.; Xiao, Z.; Huang, J.; Zhou, G.; Zhou, T.; Liu, G.; Li, Z., *Chemical Engineering Journal* **2024,** *498*, 155432. DOI https://doi.org/10.1016/j.cej.2024.155432.

42. Xu, M.-Y.; Zeng, J.; Han, X.-H.; Wei, D.-D.; Fan, B.; Qu, X. H.; Huang, S.; Han, X.-J., *Materials & Design* **2025,** *251*, 113647. DOI https://doi.org/10.1016/j.matdes.2025.113647.
43. Jiang, Y.; Li, Y.; Wang, Y.; Li, X., *Biochemical Pharmacology* **2024,** *227*, 116456. DOI https://doi.org/10.1016/j.bcp.2024.116456.
44. Zhang, L.; Yi, B.; Chen, J., *Arabian Journal of Chemistry* **2024,** *17* (9), 105861. DOI https://doi.org/10.1016/j.arabjc.2024.105861.
45. Wang, Z.; Guo, Y.; Li, K.; Huo, Y.; Wang, S.; Dong, S.; Ma, M., *Bioorganic & Medicinal Chemistry* **2024,** *115*, 117908. DOI https://doi.org/10.1016/j.bmc.2024.117908.
46. Shafie, S. M.; Liotta, L. A., *Cancer Letters* **1980,** *11* (2), 81-87. DOI https://doi.org/10.1016/0304-3835(80)90097-X.
47. Yu, B.; Liu, M.; Jiang, L.; Xu, C.; Hu, H.; Huang, T.; Xu, D.; Wang, N.; Li, Q.; Tang, B. Z.; Huang, X.; Zhang, W., *Advanced Healthcare Materials* **2024,** *13* (11), 2303643. DOI https://doi.org/10.1002/adhm.202303643.
48. Jin, L.; Zhou, S.; Zhang, T.; Cui, F.; Yu, H.; Wang, J.; Wu, M.; Wang, Y.; Song, S.; Zhang, S., *Small* **2025,** *21* (2), 2408639.
49. Rajabzadeh, P.; Zoorazma, P.; Abbasi, M.; Sadat Shandiz, S. A., *Scientific Reports* **2025,** *15* (1), 1-16.
50. Chang, Y.; Shen, S.; Zhang, L.; Zeng, J.; Sun, J.; Guo, Y.-W.; Su, M.-z., *Chemistry & Biodiversity*, e202500114.
51. Carvalho, E.; Canberk, S.; Schmitt, F.; Vale, N., *Cancers* **2025,** *17* (7), 1102.
52. Arora, R.; Yates, C.; Gary, B. D.; McClellan, S.; Tan, M.; Xi, Y.; Reed, E.; Piazza, G. A.; Owen, L. B.; Dean-Colomb, W., *PLoS One* **2014,** *9* (6), e98370.
53. Hormozi-Moghaddam, Z.; Neshasteh-Riz, A.; Taheri, S. M.; Amini, S. M.; Sedghinezhad, E., *IET nanobiotechnology* **2025,** *2025* (1), 7036856.
54. Nezhadhossein, B.; Afshar, A. S.; Homayouni Tabrizi, M.; Nematpour, F. S.; Mohtashami, M., *Scientific Reports* **2025,** *15* (1), 25473.
55. Fakudze, N.; Sarbadhikary, P.; Abrahamse, H.; George, B. P., *Advances in Traditional Medicine* **2025**, 1-19.
56. Bouttier-Figueroa, D. C.; Loreto-Romero, M. A.; González-Gutiérrez, F. H.; Cortez-Valadez, M.; Flores-Acosta, M.; Meneses-Sagrero, S. E.; Robles-Zepeda, R. E., *Preparative Biochemistry & Biotechnology* **2025,** *55* (6), 684-695.

57. Li, R.-T.; Zhu, Y.-D.; Li, W.-Y.; Hou, Y.-K.; Zou, Y.-M.; Zhao, Y.-H.; Zou, Q.; Zhang, W.-H.; Chen, J.-X., *Journal of Nanobiotechnology* **2022,** *20* (1), 212. DOI 10.1186/s12951-022-01427-4.

58. Mohan, H.; Ramalingam, V.; Lim, J.-M.; Lee, S.-W.; Kim, J.; Lee, J.-H.; Park, Y.-J.; Seralathan, K.-K.; Oh, B.-T., *Colloids and Surfaces A: Physicochemical and Engineering Aspects* **2020,** *607*, 125469. DOI https://doi.org/10.1016/j.colsurfa.2020.125469.

59. Varunkumar, K.; Anusha, C.; Saranya, T.; Ramalingam, V.; Raja, S.; Ravikumar, V., *Process Biochemistry* **2020,** *94*, 349-358.

60. Liu, G.; Gao, N.; Zhou, Y.; Nie, J.; Cheng, W.; Luo, M.; Mei, L.; Zeng, X.; Deng, W. Polydopamine-Based "Four-in-One" Versatile Nanoplatforms for Targeted Dual Chemo and Photothermal Synergistic Cancer Therapy *Pharmaceutics* [Online], **2019**.

61. Rizzk, Y. W.; El-Deen, I. M.; Behery, M. E.; Mourad, A. A. E.; Mohammed, F. Z., *Chemical Biology & Drug Design* **2024,** *103* (2), e14452. DOI https://doi.org/10.1111/cbdd.14452.

62. Younis, N. S.; Ghanim, A. M. H., *Cell Biochemistry and Biophysics* **2022,** *80* (1), 191-202. DOI 10.1007/s12013-022-01064-6.

63. Bergmeyer, H.-U., *Methods of enzymatic analysis*. Elsevier: **2012**.

GRAPHICAL ABSTRACT
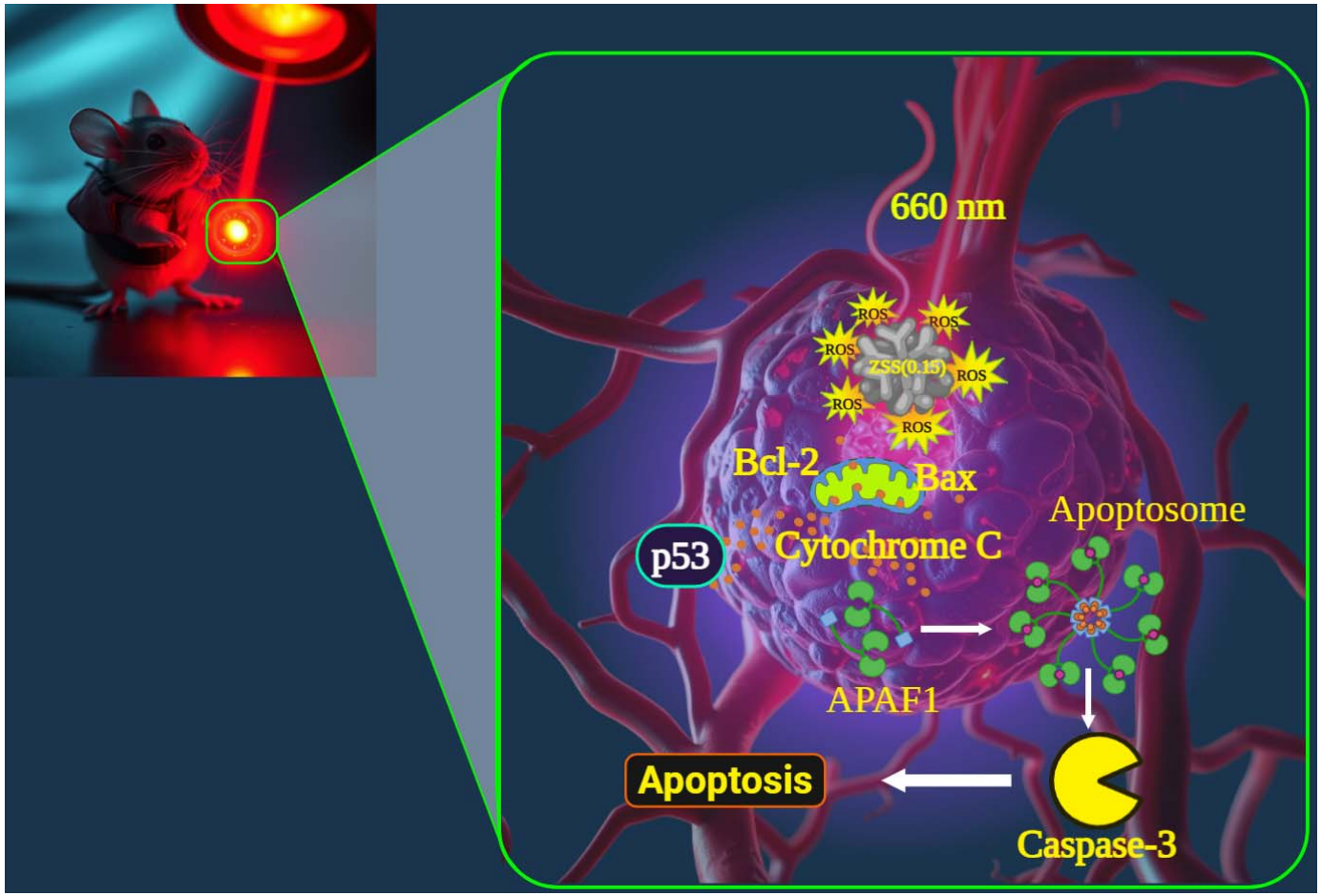
A Zn-doped Ag 2 S nanoplatform (ZSS(0.15)) enables synergistic photothermal and photodynamic therapy under 660-nm laser irradiation, triggering p53-mediated mitochondrial apoptosis via ROS generation and caspase-3 activation, achieving ~97% tumor regression *in-vivo* without detectable systemic toxicity.